PHYSICAL REVIEW C **87**, 034911 (2013)

Neutral pion production with respect to centrality and reaction plane in Au + Au collisions at $\sqrt{s_{NN}} = 200$ GeV

A. Adare,[13] S. Afanasiev,[30] C. Aidala,[43,44] N. N. Ajitanand,[62] Y. Akiba,[56,57] H. Al-Bataineh,[50] J. Alexander,[62] K. Aoki,[35,56] Y. Aramaki,[12] E. T. Atomssa,[36] R. Averbeck,[63] T. C. Awes,[52] B. Azmoun,[7] V. Babintsev,[24] M. Bai,[6] G. Baksay,[20] L. Baksay,[20] K. N. Barish,[8] B. Bassalleck,[49] A. T. Basye,[1] S. Bathe,[5,8] V. Baublis,[55] C. Baumann,[45] A. Bazilevsky,[7] S. Belikov,[7,*] R. Belmont,[67] R. Bennett,[63] A. Berdnikov,[59] Y. Berdnikov,[59] A. A. Bickley,[13] J. S. Bok,[71] K. Boyle,[63] M. L. Brooks,[39] H. Buesching,[7] V. Bumazhnov,[24] G. Bunce,[7,57] S. Butsyk,[39] C. M. Camacho,[39] S. Campbell,[63] C.-H. Chen,[63] C. Y. Chi,[14] M. Chiu,[7] I. J. Choi,[71] R. K. Choudhury,[4] P. Christiansen,[41] T. Chujo,[66] P. Chung,[62] O. Chvala,[8] V. Cianciolo,[52] Z. Citron,[63] B. A. Cole,[14] M. Connors,[63] P. Constantin,[39] M. Csanád,[18] T. Csörgő,[70] T. Dahms,[63] S. Dairaku,[35,56] I. Danchev,[67] K. Das,[21] A. Datta,[43] G. David,[7] A. Denisov,[24] A. Deshpande,[57,63] E. J. Desmond,[7] O. Dietzsch,[60] A. Dion,[63] M. Donadelli,[60] O. Drapier,[36] A. Drees,[63] K. A. Drees,[6] J. M. Durham,[63] A. Durum,[24] D. Dutta,[4] S. Edwards,[21] Y. V. Efremenko,[52] F. Ellinghaus,[13] T. Engelmore,[14] A. Enokizono,[38] H. En'yo,[56,57] S. Esumi,[66] B. Fadem,[46] D. E. Fields,[49] M. Finger,[9] M. Finger, Jr.,[9] F. Fleuret,[36] S. L. Fokin,[34] Z. Fraenkel,[69,*] J. E. Frantz,[51,63] A. Franz,[7] A. D. Frawley,[21] K. Fujiwara,[56] Y. Fukao,[56] T. Fusayasu,[48] I. Garishvili,[64] A. Glenn,[13] H. Gong,[63] M. Gonin,[36] Y. Goto,[56,57] R. Granier de Cassagnac,[36] N. Grau,[2,14] S. V. Greene,[67] M. Grosse Perdekamp,[25,57] T. Gunji,[12] H.-Å. Gustafsson,[41,*] J. S. Haggerty,[7] K. I. Hahn,[19] H. Hamagaki,[12] J. Hamblen,[64] R. Han,[54] J. Hanks,[14] E. P. Hartouni,[38] E. Haslum,[41] R. Hayano,[12] X. He,[22] M. Heffner,[38] T. K. Hemmick,[63] T. Hester,[8] J. C. Hill,[28] M. Hohlmann,[20] W. Holzmann,[14] K. Homma,[23] B. Hong,[33] T. Horaguchi,[23] D. Hornback,[64] S. Huang,[67] T. Ichihara,[56,57] R. Ichimiya,[56] J. Ide,[46] Y. Ikeda,[66] K. Imai,[29,35,56] M. Inaba,[66] D. Isenhower,[1] M. Ishihara,[56] T. Isobe,[12,56] M. Issah,[67] A. Isupov,[30] D. Ivanischev,[55] B. V. Jacak,[63,†] J. Jia,[7,62] J. Jin,[14] B. M. Johnson,[7] K. S. Joo,[47] D. Jouan,[53] D. S. Jumper,[1] F. Kajihara,[12] S. Kametani,[56] N. Kamihara,[57] J. Kamin,[63] J. H. Kang,[71] J. Kapustinsky,[39] K. Karatsu,[35,56] D. Kawall,[43,57] M. Kawashima,[56,58] A. V. Kazantsev,[34] T. Kempel,[28] A. Khanzadeev,[55] K. M. Kijima,[23] B. I. Kim,[33] D. H. Kim,[47] D. J. Kim,[31] E. Kim,[61] E.-J. Kim,[10] S. H. Kim,[71] Y. J. Kim,[25] E. Kinney,[13] K. Kiriluk,[13] Á. Kiss,[18] E. Kistenev,[7] L. Kochenda,[55] B. Komkov,[55] M. Konno,[66] J. Koster,[25] D. Kotchetkov,[49] A. Kozlov,[69] A. Král,[15] A. Kravitz,[14] G. J. Kunde,[39] K. Kurita,[56,58] M. Kurosawa,[56] Y. Kwon,[71] G. S. Kyle,[50] R. Lacey,[62] Y. S. Lai,[14] J. G. Lajoie,[28] A. Lebedev,[28] D. M. Lee,[39] J. Lee,[19] K. Lee,[61] K. B. Lee,[33] K. S. Lee,[33] M. J. Leitch,[39] M. A. L. Leite,[60] E. Leitner,[67] B. Lenzi,[60] X. Li,[11] P. Liebing,[57] L. A. Linden Levy,[13] T. Liška,[15] A. Litvinenko,[30] H. Liu,[39,50] M. X. Liu,[39] B. Love,[67] R. Luechtenborg,[45] D. Lynch,[7] C. F. Maguire,[67] Y. I. Makdisi,[6] A. Malakhov,[30] M. D. Malik,[49] V. I. Manko,[34] E. Mannel,[14] Y. Mao,[54,56] H. Masui,[66] F. Matathias,[14] M. McCumber,[63] P. L. McGaughey,[39] N. Means,[63] B. Meredith,[25] Y. Miake,[66] A. C. Mignerey,[42] P. Mikeš,[9,27] K. Miki,[56,66] A. Milov,[7] M. Mishra,[3] J. T. Mitchell,[7] A. K. Mohanty,[4] Y. Morino,[12] A. Morreale,[8] D. P. Morrison,[7] T. V. Moukhanova,[34] J. Murata,[56,58] S. Nagamiya,[32] J. L. Nagle,[13] M. Naglis,[69] M. I. Nagy,[18] I. Nakagawa,[56,57] Y. Nakamiya,[23] T. Nakamura,[23,32] K. Nakano,[56,65] J. Newby,[38] M. Nguyen,[63] T. Niida,[66] R. Nouicer,[7] A. S. Nyanin,[34] E. O'Brien,[7] S. X. Oda,[12] C. A. Ogilvie,[28] M. Oka,[66] K. Okada,[57] Y. Onuki,[56] A. Oskarsson,[41] M. Ouchida,[23,56] K. Ozawa,[12] R. Pak,[7] V. Pantuev,[26,63] V. Papavassiliou,[50] I. H. Park,[19] J. Park,[61] S. K. Park,[33] W. J. Park,[33] S. F. Pate,[50] H. Pei,[28] J.-C. Peng,[25] H. Pereira,[16] V. Peresedov,[30] D. Yu. Peressounko,[34] C. Pinkenburg,[7] R. P. Pisani,[7] M. Proissl,[63] M. L. Purschke,[7] A. K. Purwar,[39] H. Qu,[22] J. Rak,[31] A. Rakotozafindrabe,[36] I. Ravinovich,[69] K. F. Read,[52,64] K. Reygers,[45] V. Riabov,[55] Y. Riabov,[55] E. Richardson,[42] D. Roach,[67] G. Roche,[40] S. D. Rolnick,[8] M. Rosati,[28] C. A. Rosen,[13] S. S. E. Rosendahl,[41] P. Rosnet,[40] P. Rukoyatkin,[30] P. Ružička,[27] B. Sahlmueller,[45,63] N. Saito,[32] T. Sakaguchi,[7] K. Sakashita,[56,65] V. Samsonov,[55] S. Sano,[12,68] T. Sato,[66] S. Sawada,[32] K. Sedgwick,[8] J. Seele,[13] R. Seidl,[25] A. Yu. Semenov,[28] R. Seto,[8] D. Sharma,[69] I. Shein,[24] T.-A. Shibata,[56,65] K. Shigaki,[23] M. Shimomura,[66] K. Shoji,[35,56] P. Shukla,[4] A. Sickles,[7] C. L. Silva,[60] D. Silvermyr,[52] C. Silvestre,[16] K. S. Sim,[33] B. K. Singh,[3] C. P. Singh,[3] V. Singh,[3] M. Slunečka,[9] R. A. Soltz,[38] W. E. Sondheim,[39] S. P. Sorensen,[64] I. V. Sourikova,[7] N. A. Sparks,[1] P. W. Stankus,[52] E. Stenlund,[41] S. P. Stoll,[7] T. Sugitate,[23] A. Sukhanov,[7] J. Sziklai,[70] E. M. Takagui,[60] A. Taketani,[56,57] R. Tanabe,[66] Y. Tanaka,[48] K. Tanida,[35,56,57] M. J. Tannenbaum,[7] S. Tarafdar,[3] A. Taranenko,[62] P. Tarján,[17] H. Themann,[63] T. L. Thomas,[49] M. Togawa,[35,56] A. Toia,[63] L. Tomášek,[27] H. Torii,[23] R. S. Towell,[1] I. Tserruya,[69] Y. Tsuchimoto,[23] C. Vale,[7,28] H. Valle,[67] H. W. van Hecke,[39] E. Vazquez-Zambrano,[14] A. Veicht,[25] J. Velkovska,[67] R. Vértesi,[17,70] A. A. Vinogradov,[34] M. Virius,[15] V. Vrba,[27] E. Vznuzdaev,[55] X. R. Wang,[50] D. Watanabe,[23] K. Watanabe,[66] Y. Watanabe,[56,57] F. Wei,[28] R. Wei,[62] J. Wessels,[45] S. N. White,[7] D. Winter,[14] J. P. Wood,[1] C. L. Woody,[7] R. M. Wright,[1] M. Wysocki,[13] W. Xie,[57] Y. L. Yamaguchi,[12] K. Yamaura,[23] R. Yang,[25] A. Yanovich,[24] J. Ying,[22] S. Yokkaichi,[56,57] Z. You,[54] G. R. Young,[52] I. Younus,[37,49] I. E. Yushmanov,[34] W. A. Zajc,[14] C. Zhang,[52] S. Zhou,[11] and L. Zolin[30]

(PHENIX Collaboration)

[1]*Abilene Christian University, Abilene, Texas 79699, USA*

[2]*Department of Physics, Augustana College, Sioux Falls, South Dakota 57197, USA*

[3]*Department of Physics, Banaras Hindu University, Varanasi 221005, India*

[4]*Bhabha Atomic Research Centre, Bombay 400 085, India*

[5]*Baruch College, City University of New York, New York, New York 10010, USA*

[6]*Collider-Accelerator Department, Brookhaven National Laboratory, Upton, New York 11973-5000, USA*

[7]*Physics Department, Brookhaven National Laboratory, Upton, New York 11973-5000, USA*

[8]University of California-Riverside, Riverside, California 92521, USA
[9]Charles University, Ovocný trh 5, Praha 1, 116 36 Prague, Czech Republic
[10]Chonbuk National University, Jeonju 561-756, Korea
[11]Science and Technology on Nuclear Data Laboratory, China Institute of Atomic Energy, Beijing 102413, People's Republic of China
[12]Center for Nuclear Study, Graduate School of Science, University of Tokyo, 7-3-1 Hongo, Bunkyo, Tokyo 113-0033, Japan
[13]University of Colorado, Boulder, Colorado 80309, USA
[14]Columbia University, New York, New York 10027, USA and Nevis Laboratories, Irvington, New York 10533, USA
[15]Czech Technical University, Zikova 4, 166 36 Prague 6, Czech Republic
[16]Dapnia, CEA Saclay, F-91191 Gif-sur-Yvette, France
[17]Debrecen University, H-4010 Debrecen, Egyetem tér 1, Hungary
[18]ELTE, Eötvös Loránd University, H-1117 Budapest, Pázmány P. s. 1/A, Hungary
[19]Ewha Womans University, Seoul 120-750, Korea
[20]Florida Institute of Technology, Melbourne, Florida 32901, USA
[21]Florida State University, Tallahassee, Florida 32306, USA
[22]Georgia State University, Atlanta, Georgia 30303, USA
[23]Hiroshima University, Kagamiyama, Higashi-Hiroshima 739-8526, Japan
[24]IHEP Protvino, State Research Center of Russian Federation, Institute for High Energy Physics, Protvino 142281, Russia
[25]University of Illinois at Urbana-Champaign, Urbana, Illinois 61801, USA
[26]Institute for Nuclear Research of the Russian Academy of Sciences, Prospekt 60-Letiya Oktyabrya 7a, Moscow 117312, Russia
[27]Institute of Physics, Academy of Sciences of the Czech Republic, Na Slovance 2, 182 21 Prague 8, Czech Republic
[28]Iowa State University, Ames, Iowa 50011, USA
[29]Advanced Science Research Center, Japan Atomic Energy Agency, 2-4 Shirakata Shirane, Tokai-mura, Naka-gun, Ibaraki-ken 319-1195, Japan
[30]Joint Institute for Nuclear Research, 141980 Dubna, Moscow Region, Russia
[31]Helsinki Institute of Physics and University of Jyväskylä, P.O. Box 35, FI-40014 Jyväskylä, Finland
[32]KEK, High Energy Accelerator Research Organization, Tsukuba, Ibaraki 305-0801, Japan
[33]Korea University, Seoul, 136-701, Korea
[34]Russian Research Center "Kurchatov Institute", Moscow, 123098 Russia
[35]Kyoto University, Kyoto 606-8502, Japan
[36]Laboratoire Leprince-Ringuet, Ecole Polytechnique, CNRS-IN2P3, Route de Saclay, F-91128 Palaiseau, France
[37]Physics Department, Lahore University of Management Sciences, Lahore, Pakistan
[38]Lawrence Livermore National Laboratory, Livermore, California 94550, USA
[39]Los Alamos National Laboratory, Los Alamos, New Mexico 87545, USA
[40]LPC, Université Blaise Pascal, CNRS-IN2P3, Clermont-Fd, 63177 Aubiere Cedex, France
[41]Department of Physics, Lund University, Box 118, SE-221 00 Lund, Sweden
[42]University of Maryland, College Park, Maryland 20742, USA
[43]Department of Physics, University of Massachusetts, Amherst, Massachusetts 01003-9337, USA
[44]Department of Physics, University of Michigan, Ann Arbor, Michigan 48109-1040, USA
[45]Institut fur Kernphysik, University of Muenster, D-48149 Muenster, Germany
[46]Muhlenberg College, Allentown, Pennsylvania 18104-5586, USA
[47]Myongji University, Yongin, Kyonggido 449-728, Korea
[48]Nagasaki Institute of Applied Science, Nagasaki-shi, Nagasaki 851-0193, Japan
[49]University of New Mexico, Albuquerque, New Mexico 87131, USA
[50]New Mexico State University, Las Cruces, New Mexico 88003, USA
[51]Department of Physics and Astronomy, Ohio University, Athens, Ohio 45701, USA
[52]Oak Ridge National Laboratory, Oak Ridge, Tennessee 37831, USA
[53]IPN-Orsay, Universite Paris Sud, CNRS-IN2P3, BP1, F-91406 Orsay, France
[54]Peking University, Beijing 100871, People's Republic of China
[55]PNPI, Petersburg Nuclear Physics Institute, Gatchina, Leningrad Region 188300, Russia
[56]RIKEN Nishina Center for Accelerator-Based Science, Wako, Saitama 351-0198, Japan
[57]RIKEN BNL Research Center, Brookhaven National Laboratory, Upton, New York 11973-5000, USA
[58]Physics Department, Rikkyo University, 3-34-1 Nishi-Ikebukuro, Toshima, Tokyo 171-8501, Japan
[59]Saint Petersburg State Polytechnic University, St. Petersburg 195251, Russia
[60]Universidade de São Paulo, Instituto de Física, Caixa Postal 66318, São Paulo CEP 05315-970, Brazil
[61]Seoul National University, Seoul, Korea
[62]Chemistry Department, Stony Brook University, SUNY, Stony Brook, New York 11794-3400, USA
[63]Department of Physics and Astronomy, Stony Brook University, SUNY, Stony Brook, New York 11794-3400, USA
[64]University of Tennessee, Knoxville, Tennessee 37996, USA

[65]*Department of Physics, Tokyo Institute of Technology, Oh-okayama, Meguro, Tokyo 152-8551, Japan*
[66]*Institute of Physics, University of Tsukuba, Tsukuba, Ibaraki 305, Japan*
[67]*Vanderbilt University, Nashville, Tennessee 37235, USA*
[68]*Waseda University, Advanced Research Institute for Science and Engineering, 17 Kikui-cho, Shinjuku-ku, Tokyo 162-0044, Japan*
[69]*Weizmann Institute, Rehovot 76100, Israel*
[70]*Institute for Particle and Nuclear Physics, Wigner Research Centre for Physics, Hungarian Academy of Sciences (Wigner RCP, RMKI) H-1525 Budapest 114, P.O. Box 49, Budapest, Hungary*
[71]*Yonsei University, IPAP, Seoul 120-749, Korea*
(Received 12 August 2012; published 28 March 2013)

The PHENIX experiment has measured the production of π^0s in Au + Au collisions at $\sqrt{s_{NN}} = 200$ GeV. The new data offer a fourfold increase in recorded luminosity, providing higher precision and a larger reach in transverse momentum, p_T, to 20 GeV/c. The production ratio of η/π^0 is $0.46 \pm 0.01(\text{stat}) \pm 0.05(\text{syst})$, constant with p_T and collision centrality. The observed ratio is consistent with earlier measurements, as well as with the $p + p$ and d + Au values. π^0 are suppressed by a factor of 5, as in earlier findings. However, with the improved statistical precision a small but significant rise of the nuclear modification factor R_{AA} vs p_T, with a slope of $0.0106\pm^{0.0034}_{0.0029}$ (Gev/c)$^{-1}$, is discernible in central collisions. A phenomenological extraction of the average fractional parton energy loss shows a decrease with increasing p_T. To study the path-length dependence of suppression, the π^0 yield is measured at different angles with respect to the event plane; a strong azimuthal dependence of the π^0 R_{AA} is observed. The data are compared to theoretical models of parton energy loss as a function of the path length L in the medium. Models based on perturbative quantum chromodynamics are insufficient to describe the data, while a hybrid model utilizing pQCD for the hard interactions and anti-de-Sitter space/conformal field theory (AdS/CFT) for the soft interactions is consistent with the data.

DOI: 10.1103/PhysRevC.87.034911 PACS number(s): 25.75.Dw

I. INTRODUCTION

Discovery of the suppression of high-transverse-momentum (p_T) hadrons in relativistic heavy ion collisions [1–3] and the absence of such suppression in dAu collisions [4] has inspired intense theoretical work during the past decade. The phenomenon was immediately interpreted, in fact, even predicted [5–7], as the energy loss of a hard scattered parton in the hot, dense, strongly interacting quark-gluon plasma (QGP) formed in the collision. Prompted by the large amount of very diverse experimental data from the Relativistic Heavy Ion Collider (RHIC)—namely, by suppression patterns at various collision energies, colliding systems, and centralities—several models have been developed, based mostly on perturbative quantum chromodynamics (pQCD) (see Sec. III E as well as Ref. [8]). The suppression patterns are quantified by the nuclear modification factor R_{AA}, defined for single-inclusive π^0 s as

$$R_{\text{AA}}(p_T) = \frac{\left(1/N^{\text{evt}}_{\text{AA}}\right) d^2 N^{\pi^0}_{\text{AA}}/dp_T\text{dy}}{\langle T_{\text{AB}}\rangle d^2\sigma^{\pi^0}_{\text{pp}}/dp_T\text{dy}}, \quad (1)$$

where $\sigma^{\pi^0}_{pp}$ is the production cross section of π^0 in $p + p$ collisions, $\langle T_{\text{AB}}\rangle = \langle N_{\text{coll}}\rangle / \sigma^{\text{inel}}_{pp}$ is the nuclear overlap function averaged over the relevant range of impact parameters, and $\langle N_{\text{coll}}\rangle$ is the number of binary nucleon-nucleon collisions computed with $\sigma^{\text{inel}}_{pp}$. Despite their different approaches, several models [9–12] have been able to describe the p_T and centrality dependence of R_{AA} within experimental uncertainties. At the same time, those models provided very different estimates of medium properties such as the transport coefficient $\hat{q}$, the average four-momentum transfer squared per mean free path of the outgoing parton within the medium. For this reason, R_{AA} alone does not provide sufficient constraint for extracting medium properties such as $\hat{q}$ from the theoretical predictions, because it averages the varying energy losses along many different paths of the parton in the medium.

While dihadron correlation measurements are a successful approach to constrain $\langle L\rangle$ of the parton in the medium [13], the single particle observable R_{AA} typically has smaller statistical errors and a higher p_T reach. In addition, if R_{AA} is measured as a function of the azimuthal angle with respect to the event plane of the collision, the average path length $\langle L\rangle$ can be constrained [14,15]. In all but the most central ion-ion collisions, the overlap region of the nuclei is not azimuthally isotropic. The average distance the parton traverses before emerging and fragmenting varies as a function of the angle with respect to the event plane. Each collision centrality $\Delta\phi$ class selects different $\langle L\rangle$ values, so the differential observable $R_{\text{AA}}(\Delta\phi)$ directly probes the path-length dependence of the energy loss.

The first measurements of azimuthal asymmetries of nuclear suppression and collective flow [14–16] used π^0 s as the probe, which has the advantage that π^0 s are relatively easy to identify over a very wide p_T range in a single detector—a crucial factor in mitigating systematic uncertainties. As pointed out in Ref. [15], both the collective flow and the azimuthal dependence of nuclear suppression can be formally defined at any p_T, but they have historically and conceptually different roots. The notion of collective flow originates in lower p_T phenomena and is usually interpreted as a *boost* to the original p_T spectrum (of partons or final-state particles) in the direction of the highest-pressure gradient. In contrast,

*Deceased.
†PHENIX spokesperson: jacak@skipper.physics.sunysb.edu

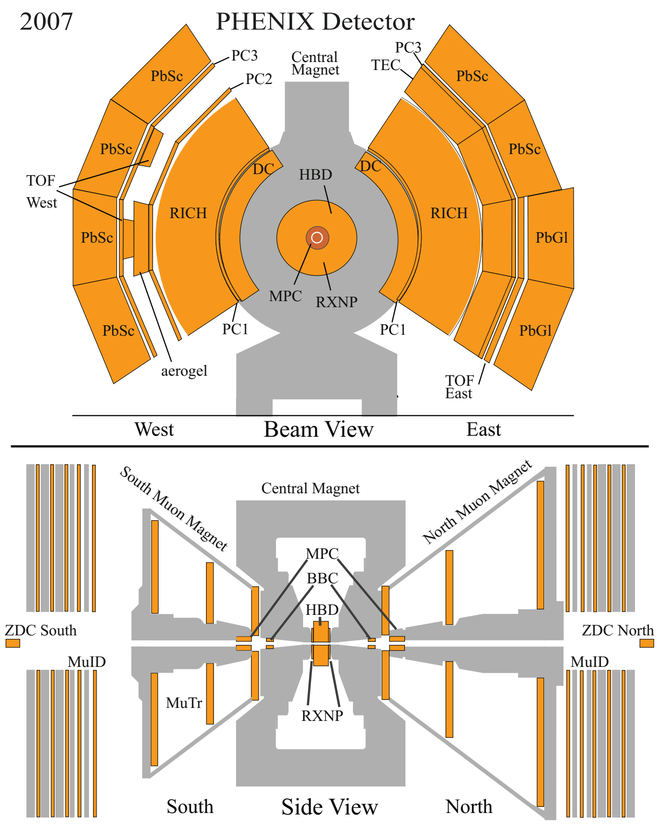

FIG. 1. (Color online) PHENIX experimental setup in the 2007 data-taking period.

R_{AA} and $R_{AA}(\Delta\phi)$ are typically used to describe high-p_T behavior, and their decrease from unity is interpreted as a *loss* of parton momentum due to the presence of a medium. In this paper, results on π^0 production and on the nuclear modification factor R_{AA} and and its azimuthal dependence in terms of the event-plane-dependent $R_{AA}(\Delta\phi)$ are presented. The results presented here are based upon the data collected in the 2007 RHIC run. The data sample is four times larger than that of Refs. [15,17]. The dedicated reaction plane detector [18] installed in 2007 offers improved event-plane resolution.

II. EXPERIMENTAL DETAILS

A. Data set

This analysis used 3.8×10^9 minimum bias Au + Au collisions at $\sqrt{s_{NN}} = 200$ GeV recorded by the PHENIX experiment [19] at RHIC in 2007. The experimental setup is shown in Fig. 1. Collision centrality was determined from the amount of charge deposited in the beam-beam counters (BBC, $3.0 < |\eta| < 3.9$). From a Monte Carlo calculation based on the Glauber model [20,21], the average number of participants N_{part}, the number of binary collisions N_{coll}, and impact parameter b were estimated (see Table I).

B. Reaction plane

Each noncentral nucleus-nucleus collision has a well-defined reaction plane, given by the beam direction and the impact parameter vector of the actual collision. Although this reaction plane cannot be directly observed, an event plane can be experimentally determined event-by-event using the method discussed in detail in Ref. [23].

TABLE I. Average N_{part}, N_{coll}, impact parameter, and participant eccentricity [22] for all centrality classes.

Centrality (%)	$\langle N_{part} \rangle$	$\langle N_{coll} \rangle$	$\langle b \rangle$ (fm)	$\langle \varepsilon_{part} \rangle$
00–10	325.8 ± 3.8	960.2 ± 96.1	3.1 ± 0.1	0.105 ± 0.004
10–20	236.1 ± 5.5	609.5 ± 59.8	5.6 ± 0.2	0.198 ± 0.008
20–30	167.6 ± 5.8	377.6 ± 36.4	7.3 ± 0.3	0.284 ± 0.010
30–40	115.5 ± 5.8	223.9 ± 23.2	8.7 ± 0.3	0.358 ± 0.011
40–50	76.2 ± 5.5	124.6 ± 14.9	9.9 ± 0.4	0.425 ± 0.013
50–60	47.1 ± 4.7	63.9 ± 9.4	10.9 ± 0.4	0.495 ± 0.016
60–70	26.7 ± 3.7	29.8 ± 5.4	11.9 ± 0.5	0.575 ± 0.023
70–80	13.7 ± 2.5	12.6 ± 2.8	12.6 ± 0.8	0.671 ± 0.024
80–93	5.6 ± 0.8	4.2 ± 0.8	13.9 ± 0.5	0.736 ± 0.021

To reduce the biases to the event-plane determination from physical correlations such as Hanbury-Brown-Twiss (HBT), resonance decay, and especially high-p_T jet production, it is necessary that the event plane be determined with a large pseudorapidity gap with respect to the high-p_T measurement [24]. Therefore, in this analysis measurements from two detectors were combined, located along the beam direction to the north and south of the interaction region. The first is a pair of muon-piston calorimeters (MPCs) [25,26] covering $3.1 < |\eta| < 3.9$ in pseudorapidity and consisting of 240 $2.2 \times 2.2 \times 18$ cm^3 $PbWO_4$ crystals each. The second is a pair of reaction-plane detectors (RxNPs) [18], which are plastic scintillators, with 20 mm of lead converter in front of them. The RxNPs are divided into 12 azimuthal segments and further divided radially into outer (RxNPout) and inner (RxNPin) rings. The outer ring covers $1.0 < |\eta| < 1.5$ and the inner ring covers $1.5 < |\eta| < 2.8$. The current analysis did not use RxNPout and the event plane was established only from the MPCs and RxNPin. The resolution is shown in Fig. 2. The method to establish the event plane from the combined MPC-RxNPin information is identical to that used in Ref. [16].

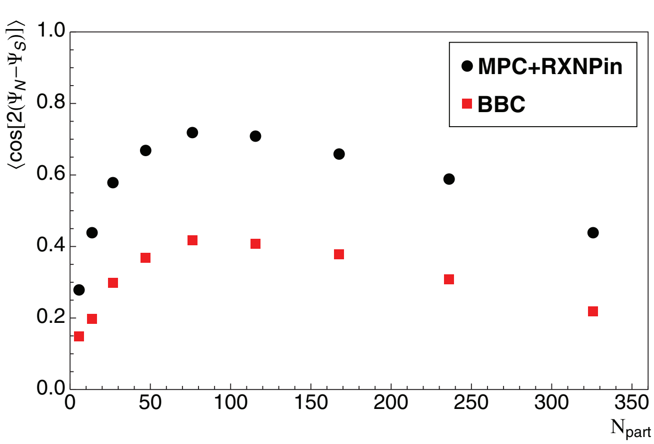

FIG. 2. (Color online) Event plane resolution as a function of collision centrality expressed in terms of N_{part}, using only the BBC and using the combined MPC and RxNPin detectors.

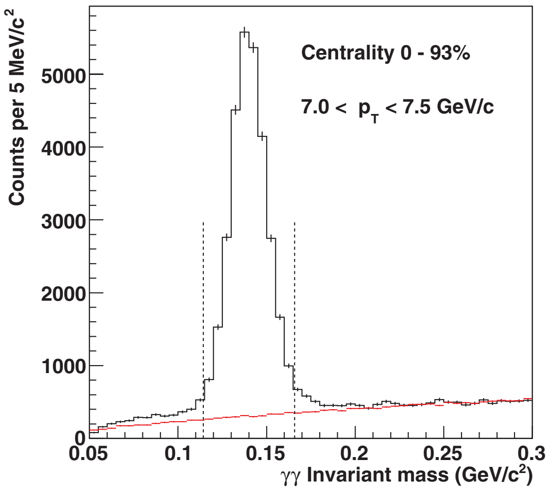

FIG. 3. (Color online) Invariant mass spectrum of two photons (black) and the corresponding mixed events (red) at $7 < p_T < 7.5$ GeV/c in minimum bias collisions. Vertical lines indicate a $\pm 2.5\sigma$ integration window.

To estimate the resolution of the event plane, it is measured independently by the north and south detectors, Ψ_N and Ψ_S, respectively. The resolution is then characterized by $\langle \cos[2(\Psi_N - \Psi_S)] \rangle$. Higher values indicate better resolution. The resolution is centrality dependent, as shown in Fig. 2.

C. Neutral pions

Neutral pions are measured via the $\pi^0 \to \gamma\gamma$ decay channel. Photons are identified in the PHENIX electromagnetic calorimeter (EMCal, described in Ref. [27]) consisting of two subdetectors, both extending to $|\eta| < 0.35$ in pseudorapidity and are located at 5.1 m radial distance from the collision point. This analysis uses data from the lead-scintillator (PbSc) sampling calorimeter, which comprises six sectors covering 3/8 of the full azimuth and has a 5.5×5.5 cm^2 granularity and a depth of 18 radiation lengths. Photons are identified using various cuts on the shower shape observed in the calorimeter as well as by comparing the observed shapes to an ideal one, parametrized using well-controlled test beam data [27]. Because this analysis is restricted to the p_T region above 5 GeV/c, the hadron contamination is small; hadrons in this energy region typically deposit only a small fraction of their energy in the EMCal.

The invariant mass $m_{\gamma\gamma}$ is calculated in bins of photon pair p_T from each pair of photons, provided the pair passes the energy asymmetry cut $\alpha < 0.8$, where $\alpha = |E_{\gamma_1} - E_{\gamma_2}|/(E_{\gamma_1} + E_{\gamma_2})$ and the distance between the impact positions of the two photons is larger than 8 cm. An example $m_{\gamma\gamma}$ distribution is shown in Fig. 3. For the event-plane-dependent studies the procedure is repeated in six 15°-wide bins of angles $\Delta\phi$ with respect to the event plane. The combinatorial background is estimated with the event-mixing technique where photons from one event are combined with photons from other events, which satisfy the same global conditions (vertex position, centrality, event-plane direction), and $m_{\gamma\gamma}$ is calculated. The mixed-event $m_{\gamma\gamma}$ distributions are then normalized and subtracted from the real-event distributions. The resulting π^0 peaks are $\sigma = 10$–11 MeV wide, depending on centrality, and have a very small residual background due to the inherent correlations in real events not reproducible by the mixed-event technique. This residual background is fitted to a second-order polynomial in the regions below and above the π^0 peak. This polynomial shape is then subtracted from the $m_{\gamma\gamma}$ distribution. The raw π^0 yields are extracted by integrating the resulting histogram in a $\pm 2.5\sigma$-wide $m_{\gamma\gamma}$ window.

To establish the combined effects of acceptance and π^0 detection efficiency, single π^0 s are generated with a distribution uniform in ϕ and extending to $|\eta| < 0.5$ in pseudorapidity and then are simulated in the full GEANT3 [28] framework of PHENIX. After the GEANT3 output is tuned to reproduce the inactive detector areas as well as the peak positions and widths observed in real data, the simulated π^0 s are embedded into real events. The embedded output can then be analyzed with the very same tools as the real events.

At high p_T, the two decay photons may be so close that the EMCal can no longer resolve them as two particles and provide the proper energies and impact points. The two photons "merge" into one cluster, and the corresponding π^0 cannot be reconstructed from $m_{\gamma\gamma}$. Such merged clusters are rejected by various shower profile cuts, and the loss is determined by simulated π^0 s embedded into real events and analyzed with the same cuts. At 11 GeV/c merging happens only for the most symmetric decays resulting in a 5% loss of π^0 s. At 17 GeV/c the correction is 50%. At $p_T = 20$ GeV/c about 70% of π^0 s are lost due to this effect. The systematic uncertainties are estimated by comparing π^0 yields extracted in bins of asymmetry (α). The π^0 yields are corrected for the p_T bin width by fitting the invariant yield to a power-law fit and adjusting the yield to correspond to the one at the center of the p_T bin.

D. Systematic uncertainties

Systematic uncertainties are characterized as follows. Type A uncertainties are point-to-point uncorrelated with p_T. Type B uncertainties have point-to-point correlations that cannot be characterized by a simple multiplicative factor, but vary smoothly with p_T. Finally, type C uncertainties would move all points up or down by a common multiplicative factor, a typical example being the uncertainty on $N_{\rm coll}$ in $R_{\rm AA}$.

The type B systematic uncertainty of the π^0 raw yield extraction is estimated by comparing yields obtained in windows of varying widths. The uncertainty is less than 5% for peripheral collisions (low multiplicity, small combinatorics) and reaches about 7% in central collisions.

The uncertainty on the efficiency of the photon identification (PID) is estimated comparing fully corrected π^0 yields obtained with various PID cuts. The uncertainty is 2–4% at 5–8 GeV/c and increases both with centrality and with p_T. It is of type B.

The uncertainty on the energy scale is estimated from how well the peaks and widths of simulated π^0 s embedded in real events agree with the measured peaks and widths at each centrality. The difference is less than 1% at 5–8 GeV/c. Due to the steeply falling π^0 spectrum this less-than-1% uncertainty of the energy scale translates to about 7% uncertainty on the π^0 invariant yield.

The uncertainty due to the photon-merging correction is estimated as follows. Raw yields at high p_T are extracted in different asymmetry windows both from real data and simulated decay photon pairs embedded in real data. Apart from small and precisely calculable acceptance effects, the true asymmetry distribution is flat, and at any given p_T one should observe the same raw π^0 yield, for instance, in the windows $0.4 < \alpha < 0.6$ and $0.6 < \alpha < 0.8$. However, lower asymmetry means a smaller opening angle of the decay leading to a greater probability for the photons to merge. Therefore, the measured asymmetry distribution at high p_T is not flat. To determine the photon-merging correction and its systematic uncertainty, a series of raw yield ratios in different asymmetry bins is compared between data and simulation. The uncertainties on the π^0 spectra due to the merging correction are p_T and centrality dependent.

The uncertainty due to acceptance corrections is estimated from the ratio of simulated acceptance distribution and its fit function, which is actually used for corrections. Because the geometry is well understood and a single map to exclude malfunctioning areas of the detector is used for the entire data set, this uncertainty is less than 1% for all centralities.

There are two sources of π^0 s not coming from the vertex (off-vertex π^0): those produced by hadrons interacting with detector material (instrumental background) and feed-down products from weak decay of higher-mass hadrons (physics background). Based upon simulations, both types of background are found to be negligible at less than 1% for p_T greater than 2.0 GeV/c, with the exception of π^0 s from K_s^0 decay which contribute about 3% to the π^0 yield for p_T greater than 1 GeV/c, and have been subtracted from the data. The uncertainty due to this effect is conservatively estimated as 1.5% and is of type C.

E. $R_{AA}(\Delta\phi, p_T)$

Similar to the previous analysis [15] the $R_{AA}(\Delta\phi, p_T)$ measurement uses both the inclusive $R_{AA}(p_T)$ and the quantity v_2, where v_2 is defined as the second Fourier expansion coefficient of the single inclusive azimuthal distribution:

$$\frac{dN}{d\Delta\phi} = \frac{N}{2\pi}\,[1 + 2v_2\cos(2\Delta\phi)] \tag{2}$$

and $\Delta\phi = \Psi - \phi$. This assumes that the second Fourier coefficient is dominant in this expansion. The azimuthal anisotropy v_2 is published in Ref. [16].

The π^0 yield is subdivided into six evenly spaced azimuthal bins in $\Delta\phi$ from 0 to $\pi/2$ on an event-by-event basis using the measured event plane (see Sec. II B). From the inclusive R_{AA} the $\Delta\phi$-dependent R_{AA} can be constructed as

$$R_{AA}(\Delta\phi_i, p_T) = F(\Delta\phi_i, p_T)R_{AA}(p_T), \tag{3}$$

where

$$F(\Delta\phi_i, p_T) = \frac{N(\Delta\phi_i, p_T)}{\frac{1}{n}\sum_{i=1}^{n} N(\Delta\phi_i, p_T)} \tag{4}$$

and the summation runs over the $n = 6$ azimuthal bins.

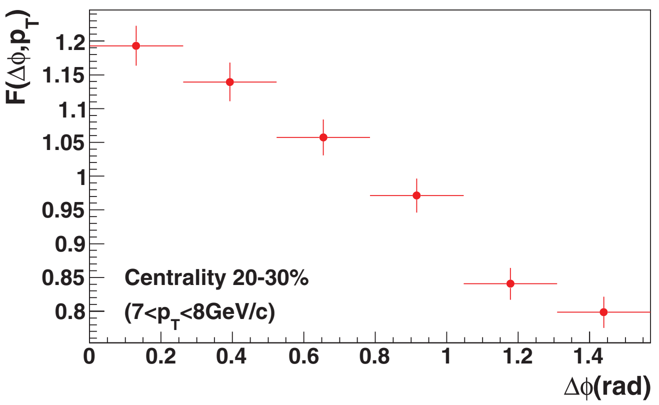

FIG. 4. (Color online) The corrected ratio $F(\Delta\phi, p_T)$ as a function of azimuthal angle at centrality 20–30%.

Because of finite event-plane resolution, $F(\Delta\phi_i, p_T)^{\text{meas}}$, as calculated from the raw yields, needs to be corrected. An approximate unfolding can be done by using the raw v_2^{raw} and the resolution-corrected v_2^{corr}

$$F(\Delta\phi_i, p_T) = F(\Delta\phi_i, p_T)^{\text{meas}} \times \frac{1 + 2v_2^{\text{corr}}\cos(2\Delta\phi)}{1 + 2v_2^{\text{raw}}\cos(2\Delta\phi)}. \tag{5}$$

The relation between the raw and the corrected v_2 is given by

$$v_2^{\text{cor}} = \frac{v_2^{\text{raw}}}{\langle\cos[2(\Psi_N - \Psi_S)]\rangle}. \tag{6}$$

The denominator is shown in Fig. 2. Figure 4 shows $F(\Delta\phi, p_T)$ at $7 < p_T < 8$ GeV/c for centrality 20–30%.

III. RESULTS

A. Spectra and power law fits

Figure 5 shows the π^0 invariant yield in Au + Au collisions for all centralities and for minimum bias data. As with earlier published π^0 results [17], in this p_T range all distributions are well described by a single power-law function [$f(p_T) = Ap_T^{-n}$]. The fit method employed here takes both statistical and systematic uncertainties into account, following the one established in previous publications [17,29,30]. The obtained fit parameters are listed in Table III for all Au + Au centrality classes, as well as for $p + p$ measured in 2005 [31]. In the more peripheral collisions the Au + Au and $p + p$ powers are consistent, but in central collisions the Au + Au powers are slightly smaller, which is also reflected in the behavior of the nuclear modification factor (see Sec. III C). Figure 6 shows the amplitudes and powers from Table III.

B. The production ratio η/π^0

Combining the current high statistics π^0 results with the published η-meson spectra from the same (2007) data set [30] provides new η/π^0 ratios with uncertainties much smaller than those published previously [32]. Figure 7 compares the measured η/π^0 ratios from minimum bias collisions for various data sets and colliding systems. Although the

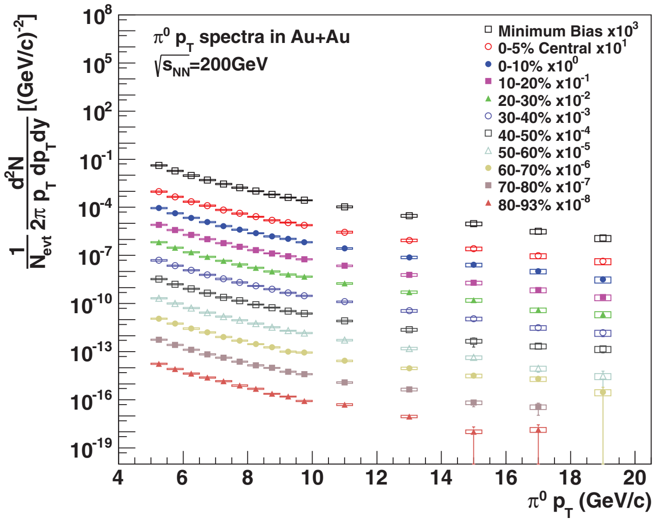

FIG. 5. (Color online) Invariant yield of π^0 as a function of p_T for each 10% centrality class, 0–5% centrality, and minimum bias. The p_T scale starts at 4 GeV/c. Error bars are the sum of statistical and type A systematic uncertainties; boxes are the sum of type B and type C systematic uncertainties.

uncertainties vary, the new ratios are consistent with previously published ones [32] and are also consistent with the overlaid PYTHIA-6.131 $p + p$ calculation.

Figure 8 shows the η/π^0 ratios for various centralities along with the PYTHIA $p + p$ values. A linear fit to the minimum bias data gives a constant term of 0.46 ± 0.05 and a slope of -0.0025 ± 0.0037, with the χ^2 contours shown in

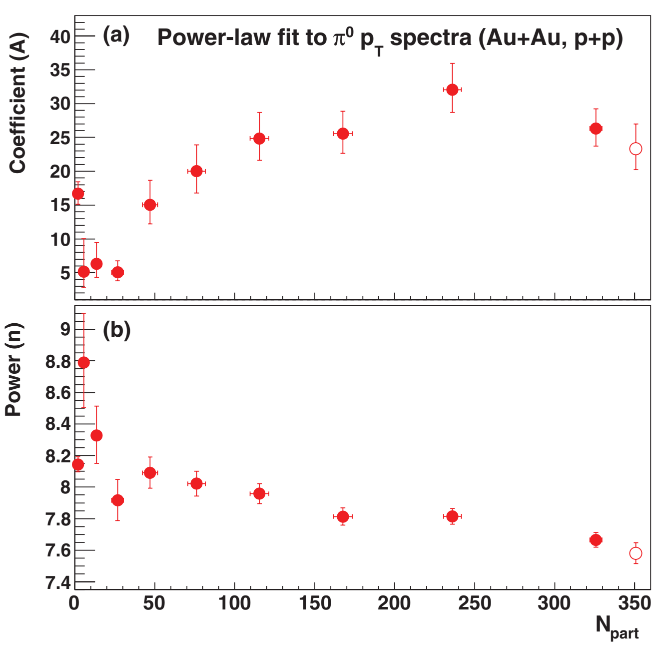

FIG. 6. (Color online) Power-law fit parameters (as tabulated in Table III) to the π^0 spectra in the 7–20 GeV/c p_T range as a function of centrality, expressed in terms of $N_{\rm part}$ and for $p + p$ (first point). Shown are (a) amplitudes and (b) powers. Note that the open points ($N_{\rm part} = 352$) correspond to 0–5% centrality and partially overlap with the adjacent points ($N_{\rm part} = 325$, 0–10%).

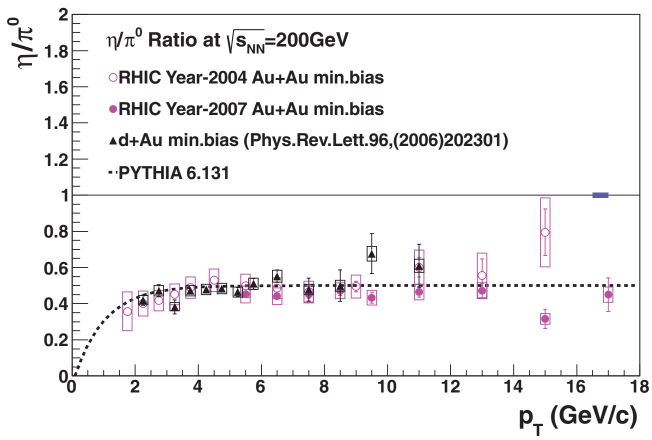

FIG. 7. (Color online) The η to π^0 ratio as a function of p_T for minimum bias Au + Au collisions in 2004 and 2007 (this analysis) data sets, dAu collisions (2003 [32]), and PYTHIA 6.131 [33]. Boxes are p_T-correlated systematic uncertainties (type B); the shaded box at 1 is the global uncertainty (type C).

Fig. 9. The fit method employed here takes both statistical and systematic uncertainties into account, following the one established in previous publications [17,29,30], and fit values for all centralities are listed in Table IV. Because the data are fully consistent with a 0 slope, they are refitted with a constant in the 5–18 GeV/c p_T range, resulting in the final values of $\eta/\pi^0 = 0.45^{+0.01}_{-0.01}$ for minimum bias, $\eta/\pi^0 = 0.47^{+0.01}_{-0.02}$ for 0–20%, $\eta/\pi^0 = 0.51^{+0.01}_{-0.01}$ for 20–60%, and $\eta/\pi^0 = 0.51^{+0.02}_{-0.02}$ for 60–93% centrality. Results of the statistical analysis of the constant fit to the minimum bias data are shown in Fig. 10. Note that the earlier published value [32] for the most-central Au + Au collisions was $\eta/\pi^0 = 0.40 \pm 0.04$; the current result is closer to the η/π^0 ratios observed in dAu (0.47 ± 0.03) and $p + p$ (0.48 ± 0.03) [32].

The lack of nuclear effects on this ratio indicate that at high p_T the fragmentation occurs outside the medium and the ratio is governed by vacuum fragmentation [32]. This is

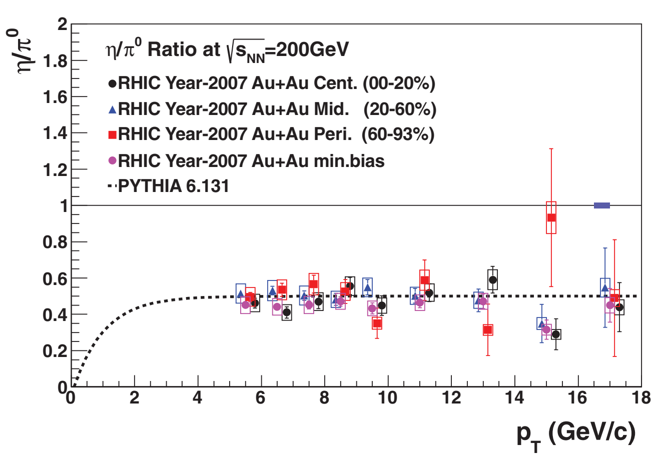

FIG. 8. (Color online) The centrality dependence for the ratio of η to π^0 as a function of p_T and the expectation from PYTHIA 6.131 [33]. Boxes are p_T-correlated systematic uncertainties (type B); the shaded box at 1 is the global uncertainty (type C).

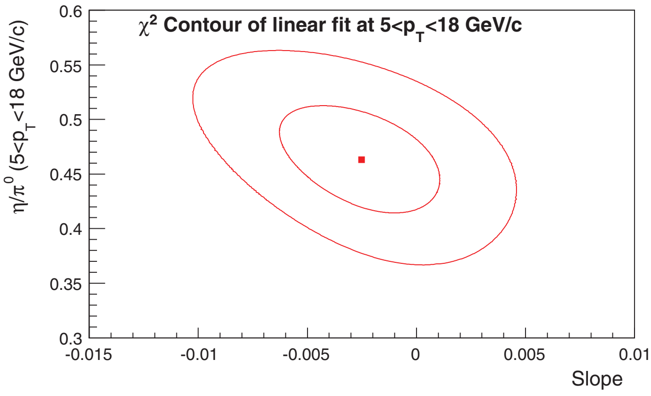

FIG. 9. (Color online) The 1σ and 2σ standard deviation χ^2 contours of the linear fit to the minimum bias η/π^0 ratio.

also supported by a recent global analysis of η fragmentation functions (consider Fig. 5 in Ref. [34] and the fact that the relevant z range, the fraction of the four-momentum of the parton taken by a fragment, in the current measurement is about 0.05–0.2). The relevant p_T is presumably 5–6 GeV/c, below which recombination may be a significant hadronization mechanism (see Refs. [35–37]). Also, it should be pointed out, that precise knowledge of the absolute value of this ratio is important for the background calculations in dielectron and direct photon measurements.

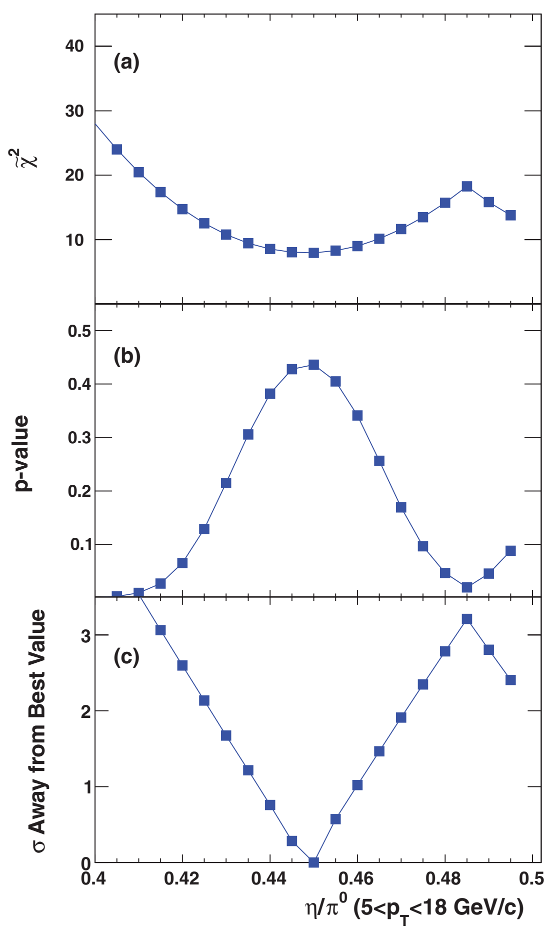

FIG. 10. (Color online) Statistical analysis of the constant fit to the minimum bias η/π^0 ratio following the method in Ref. [29].

TABLE II. Typical (minimum bias) values of systematic uncertainties of the invariant yields of π^0.

p_T (GeV/c)	Indep.	6	8	10	16	Type
Yield extraction (%)		5.0	4.0	3.0	2.0	B
E scale (%)		6.0	6.0	7.0	7.0	B
PID (%)		4.0	3.0	4.0	5.0	B
Merging (%)				4.5	28.0	B
Acceptance (%)	1.0					B
Off-vertex (%)	1.5					C
Total (%)	1.8	8.8	7.8	9.7	29.4	

C. Nuclear modification factor (ϕ integrated)

The reference yield of π^0 in $p+p$ collisions has been obtained from data taken in 2005 [31]. Instead of using a fit to the $p+p$ data, R_{AA} has been calculated by dividing the Au + Au yields point-by-point by the T_{AB}-scaled $p+p$ cross section. Figure 11 shows R_{AA} for π^0 s as a function of p_T for six representative centrality classes with the new results overlaid on the previously published ones [17]. The analysis presented here spans the range $p_T = 5$–20 GeV/c in several centrality classes. Gray bands show the global systematic uncertainties and are of type C, which are the quadratic sum of uncertainties of N_{coll}, $p+p$ normalization, and off-vertex π^0 contribution shown in Table II. The results agree well in the overlapping p_T region with the published R_{AA} data [17].

Figure 12 compares current RHIC $\sqrt{s_{NN}} = 200$ GeV Au + Au π^0 R_{AA} data to the charged hadron R_{AA} observed in $\sqrt{s_{NN}} = 2.76$ TeV Pb + Pb collisions at the Large Hadron Collider (LHC) (ALICE experiment) [38]. For the Pb + Pb points, the vertical error bars show the total errors. For both centralities and over the entire p_T range of 5–20 GeV/c, the two data sets appear to be similar. This is remarkable given the 14-fold increase of colliding energy, resulting in an approximately factor of 2 increase in the parton density at

TABLE III. Fit parameters of the power-law fit $f(p_T) = Ap_T^{-n}$ to the invariant yield ($7 < p_T < 20$ GeV/c range) in various centrality Au + Au collisions and the $p+p$ cross section [31].

System	A	n	χ^2/NDF
Au + Au 0–5%	$23.3^{+3.67}_{-3.11}$	7.58 ± 0.07	7.36/9
Au + Au 0–10%	$26.3^{+2.9}_{-2.6}$	7.66 ± 0.05	5.43/9
Au + Au 10–20%	$32.1^{+3.9}_{-3.4}$	7.81 ± 0.05	1.38/9
Au + Au 20–30%	$25.6^{+3.3}_{-2.9}$	$7.81^{+0.06}_{-0.05}$	14.2/9
Au + Au 30–40%	$24.9^{+3.9}_{-3.3}$	7.96 ± 0.06	11.3/9
Au + Au 40–50%	$20.0^{+3.9}_{-3.2}$	8.02 ± 0.08	7.50/9
Au + Au 50–60%	$15.0^{+3.6}_{-2.8}$	8.09 ± 0.10	5.56/9
Au + Au 60–70%	$5.04^{+1.73}_{-1.24}$	7.92 ± 0.13	12.6/9
Au + Au 70–80%	$6.32^{+3.12}_{-2.02}$	$8.33^{+0.19}_{-0.18}$	6.48/8
Au + Au 80–93%	$5.16^{+4.85}_{-2.38}$	$8.79^{+0.31}_{-0.29}$	8.14/8
Au + Au 0–93%	$16.4^{+0.93}_{-0.87}$	7.86 ± 0.02	11.2/9
$p+p$ (σ)	$16.7^{+1.73}_{-1.55}$	8.14 ± 0.05	15.9/9

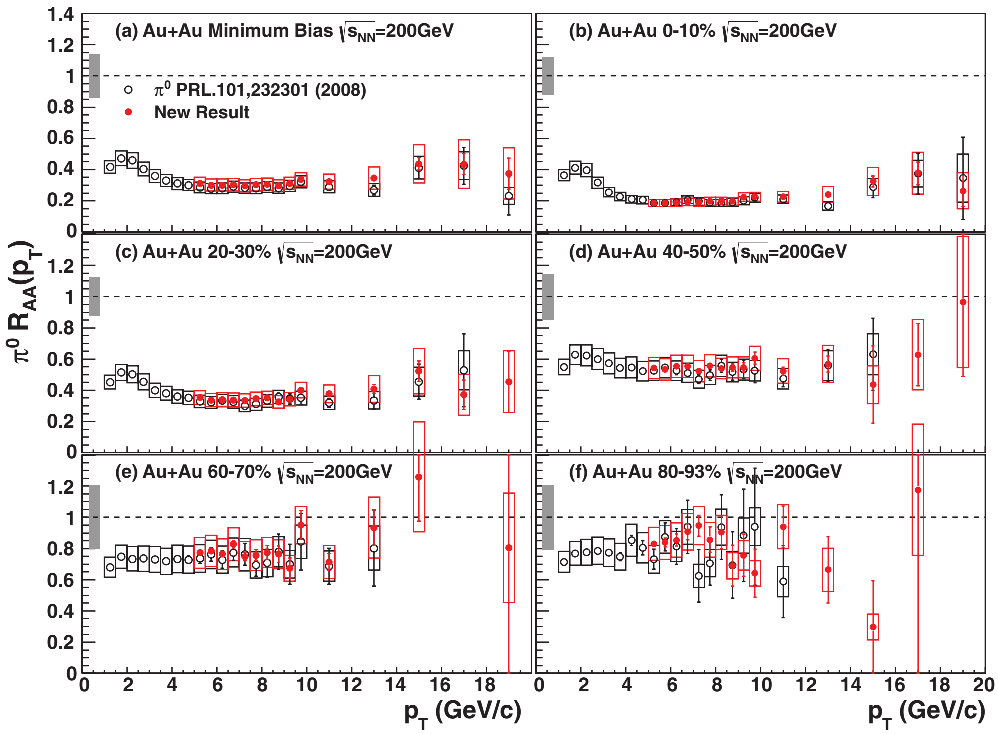

FIG. 11. (Color online) The nuclear modification factor R_{AA} of π^0 as a function of p_T for various 10%-wide centrality classes. Solid (red) circles are the results from the current analysis, while open (black) circles are the data published in Ref. [17]. Shaded (gray) boxes around 1 indicate global systematic uncertainties and are of type C. The $p + p$ reference is from the 2005 PHENIX data [31].

the LHC [39]. The expected increase in the parton density is corroborated by the factor of 2.2 increase in $dN_{\mathrm{ch}}/d\eta$ reported by ALICE [40].

However, there are two important caveats. Preliminary results from the same experiment on π^0 s, measured via photon conversions up to 10 GeV/c, show an R_{AA} that is somewhat lower in central collisions than for charged hadrons [41]. In Ref. [39] the authors assert that the similarity of R_{AA} at RHIC and the LHC may be coincidental. In any case, it does not mean that RHIC and LHC data show the same average parton energy loss $\langle\varepsilon\rangle$ (see Sec. III D), because the spectra are much harder (the power $n = 6$) at the LHC. The power is obtained by fitting the ALICE charged hadron data [38].

The fact that at $\sqrt{s_{NN}} = 200$ GeV in central collisions R_{AA} reaches its minimum around 5 GeV/c transverse momentum was first observed in Ref. [2]. At higher p_T R_{AA} appeared to be approximately constant, although the data did not unambiguously exclude a slow rise with p_T [29,30]. On the other hand, all models that reproduce the large suppression observed at p_T of 6–10 GeV/c predict a slow rise of R_{AA} as the transverse momentum increases [39,42]. The current, higher precision data are used to reassess the p_T dependence of π^0 suppression in the RHIC regime.

TABLE IV. Fit parameters of linear fit to the η/π^0 ratio in 200 GeV Au + Au collisions for various centralities.

Centrality	Intercept	Slope [(GeV/c)$^{-1}$]	χ^2/NDF
00–93%	0.463 ± 0.049	$-2.52 \times 10^{-3} \pm 3.66 \times 10^{-3}$	7.46/7
00–20%	0.463 ± 0.053	$3.33 \times 10^{-3} \pm 5.76 \times 10^{-3}$	14.8/7
20–60%	0.525 ± 0.058	$-5.67 \times 10^{-3} \pm 5.43 \times 10^{-3}$	4.03/7
60–93%	0.511 ± 0.061	$-2.80 \times 10^{-3} \pm 1.03 \times 10^{-2}$	9.36/7

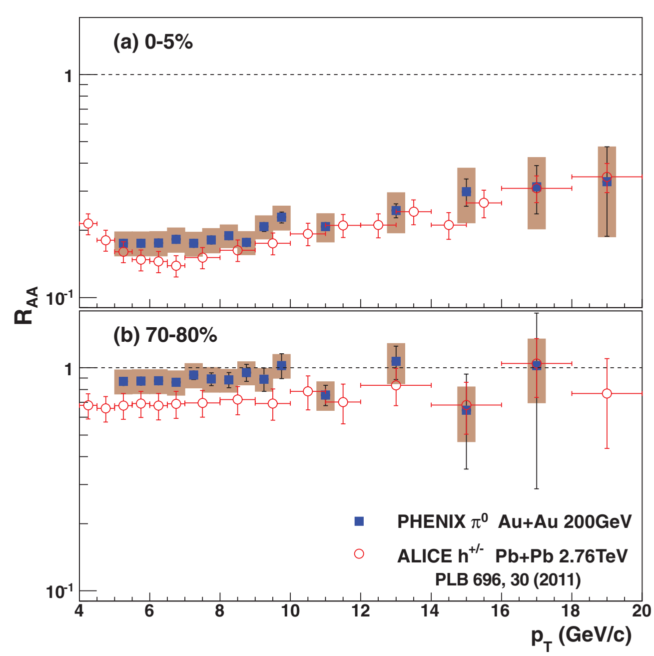

FIG. 12. (Color online) Comparison of the π^0 R_{AA} from this measurement and the charged hadron R_{AA} in Pb + Pb collisions at $\sqrt{s_{NN}} = 2.76$ TeV from the ALICE experiment [38] at LHC. The central and peripheral classes are (a) 0–5% and (b) 70–80%.

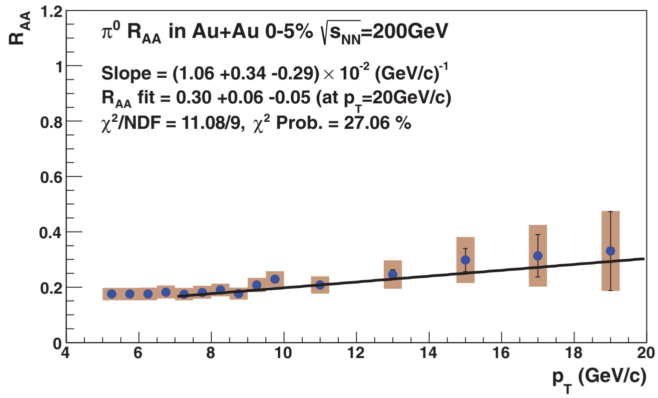

FIG. 13. (Color online) Linear fit to the p_T dependence of R_{AA} in the 7–20 GeV/c p_T range in the most central (0–5%) Au + Au collisions. Both statistical (bars) and systematic (boxes) uncertainties are considered in the fit.

Figure 13 shows a sample linear fit to the p_T dependence of R_{AA} in the most-central Au + Au data. Figure 14 shows the 1σ and 2σ contour lines of the fitted slope and intercept for three centralities. The fit method employed here takes both statistical and systematic uncertainties into account, following the one established in previous publications [17,29,30]. In contrast to Fig. 9 in Ref. [29] where the slope was consistent with 0 within 1σ due to the large uncertainties, the slope here is significantly different from 0, not only in the most-central collisions but also in the 20–30% centrality collisions.

Figure 15 shows the fitted slopes (a) and the R_{AA} from the fits (b) at 7 and 20 GeV/c for all centralities, expressed in terms of N_{part}. At and above N_{part} = 167 (20–30% centrality) the slopes are significantly different from 0.

D. Phenomenological energy loss

The average fractional momentum loss (S_{loss}) of high-p_T hadrons has been of interest because it may reflect the average fractional energy loss of the initial parton. S_{loss} is defined as $\delta p_T/p_T$, where δp_T is the difference of the momentum

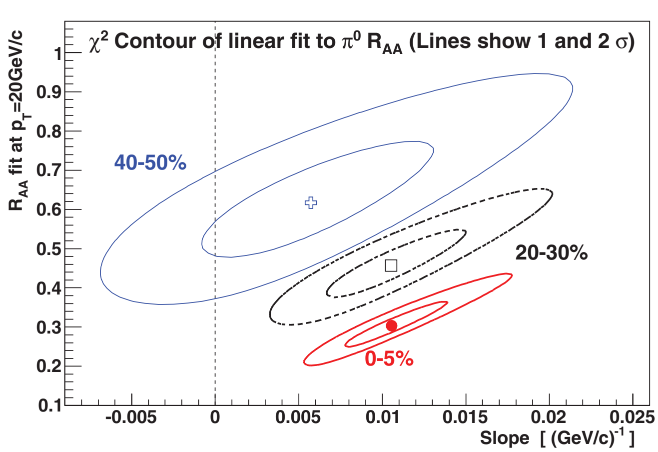

FIG. 14. (Color online) The 1σ and 2σ standard deviation χ^2 contours of the linear fit (cf. Fig. 13) to the p_T dependence of R_{AA} for three different centralities.

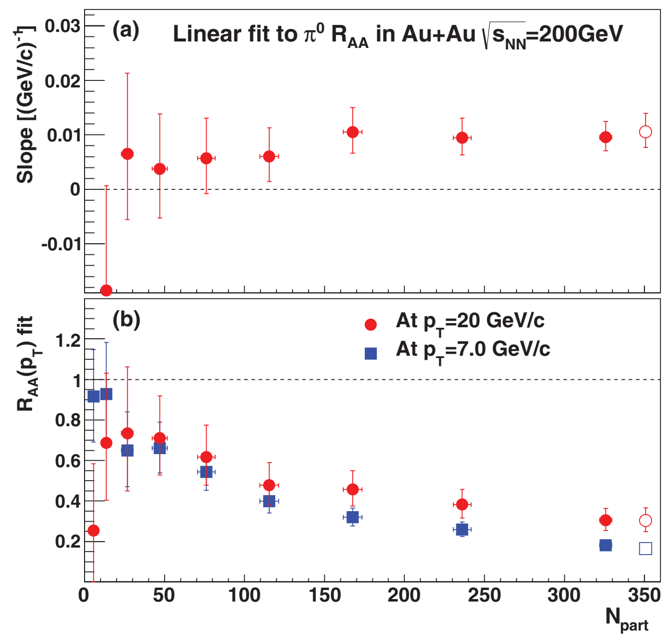

FIG. 15. (Color online) (a) Slopes of the linear fits to π^0 R_{AA} vs p_T in $\sqrt{s_{NN}} = 200$ GeV Au + Au collisions (as shown in Fig. 13) and the fitting uncertainties. The fits are in the 7–20 GeV/c p_T range. The horizontal axis is centrality, expressed in terms of N_{part}. (b) Values of R_{AA} calculated from the fits at $p_T = 7$ GeV/c and $p_T = 20$ GeV/c, also as a function of centrality. Note that the open points ($N_{part} = 352$) correspond to 0–5% centrality and partially overlap with the adjacent points ($N_{part} = 325$, 0–10%).

in $p + p$ collisions ($p_{T,pp}$) and that in Au + Au collisions [$p_{T,AuAu}$], and the p_T in the denominator is $p_{T,pp}$. In the previous publication [14], the assumption was made that both Au + Au and $p + p$ spectra are comparable in shape and R_{AA} vs p_T is flat or slowly varying, because the data sample size was not large enough to directly calculate the δp_T. With these assumptions, the suppression of high-p_T hadrons could be phenomenologically interpreted as a fractional momentum loss $\delta p_T/p_T$ by fitting Au + Au spectra with $f(p_T) = A \times [p_T(1 + \delta p_T/p_T)]^{-n}$, where A and n were obtained by fitting a power-law function to T_{AA}-scaled $p + p$ cross section [14].

With larger statistics $p + p$ and Au + Au data collected, it is possible to directly calculate S_{loss} without any assumptions. The calculation method is schematically depicted in Fig. 16. First, the π^0 cross section in $p + p$ [$f(p_T)$] is scaled by T_{AA} corresponding to the centrality selection of the Au + Au data [$g(p_T)$]. Second, the scaled $p + p$ cross section [$T_{AA} f(p_T)$] is fit with a power-law function [$h(p_T)$]. Third, the scaled $p + p$ point closest in yield to the Au + Au point of interest [$p'_{T,pp}$] is found using the fit to interpolate between T_{AA} scaled $p + p$ data points. The δp_T is calculated as $p_{T,pp} - p_{T,AuAu}$. For obtaining S_{loss}, the δp_T is divided by the $p_{T,pp}$. The uncertainty of the S_{loss} is calculated by inversely converting the quadratic sum of the uncertainties on the yields of Au + Au and $p + p$ points, by the $p + p$ fit function. Statistical and type B systematic uncertainties are individually calculated in the same way. Therefore, the p_T dependence of systematic uncertainties is propagated to the S_{loss} values.

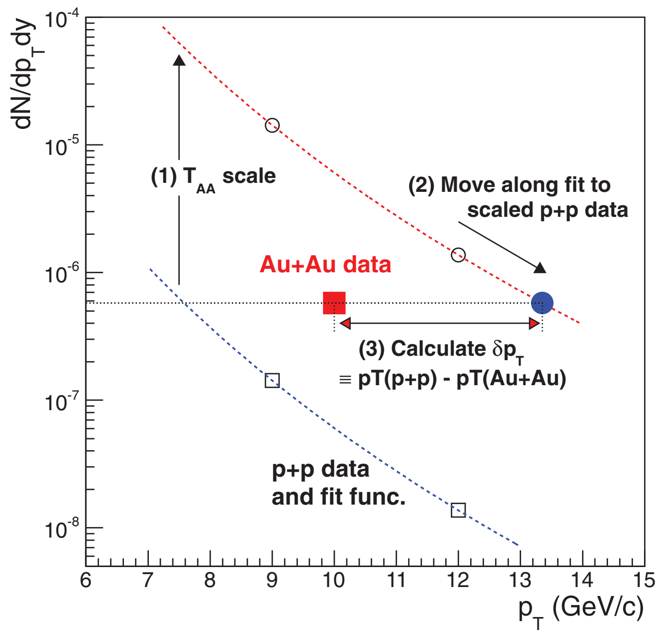

FIG. 16. (Color online) Method of calculating average fractional momentum loss ($S_{\rm loss} \equiv \delta p_T/p_T$). This plot is for illustration only; errors are not shown. In the order of procedure: (1) Scale the $p+p$ data by $T_{\rm AA}$ corresponding to centrality selection of Au + Au data, (2) shift the $p+p$ points closest to Au + Au in yield, and (3) calculate momentum difference of $p+p$ and Au + Au points.

Figure 17 shows the results for minimum bias collisions and three different centralities. The uncertainty coming from $T_{\rm AA}$, which is of type C, changes with centrality selection as listed on the plot. The $p+p$ normalization error of 9.7% is not shown here because it moves all the points independent of p_T or centrality. Because $S_{\rm loss}$ is plotted as a function of p_T in $p+p$ collisions, the p_T points in successive centrality bins in Au + Au are shifted as the momentum loss of hadrons varies. An interesting feature of the central collision data is that while $\delta p_T/p_T$ is constant up to at least 10 GeV/c, at higher p_T it slowly decreases, consistent with the slow rise of $R_{\rm AA}$. If one assumes that the fragmentation function of the parton after energy loss is unchanged, the fractional momentum loss can be interpreted as the average fractional energy loss $\langle\varepsilon\rangle = \langle\Delta E/E\rangle$ of the initial parton. This $\langle\varepsilon\rangle$ can then be compared to the trends predicted in Ref. [39]. In this particular model (see Fig. 4 in Ref. [39]), the collisional energy loss appears to be somewhat overestimated, particularly below 10 GeV/c, but at higher p_T the observed trend in $\delta p_T/p_T$ is reproduced quite well.

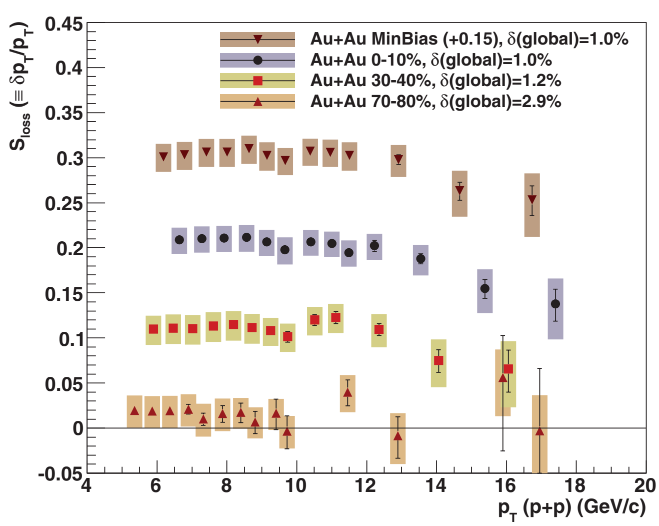

FIG. 17. (Color online) Average fractional momentum loss, as defined in the text, between various centrality Au + Au and $T_{\rm AA}$-scaled $p+p$ collisions. The horizontal axis is the p_T in the $p+p$ collision. Note that for clarity the minimum bias data are shifted up by 0.15. δ(global) stands for the uncertainty coming from the uncertainties of $T_{\rm AA}$. The overall normalization error from the $p+p$ measurement is 1.3% and is not shown here.

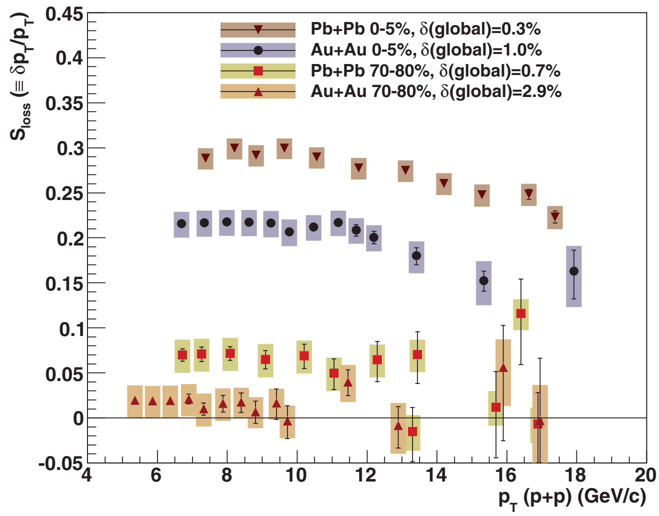

FIG. 18. (Color online) Comparison of average fractional momentum loss, as defined in the text, between the $\sqrt{s_{NN}} = 200$ GeV Au + Au collisions (π^0, current paper) and $\sqrt{s_{NN}} = 2.76$ TeV Pb + Pb collisions (ALICE, charged hadrons [38]). The centrality selections are the same. δ(global) stands for the uncertainty coming from the uncertainties of $T_{\rm AA}$. The overall normalization error from the $p+p$ measurement is 1.3% for Au + Au data and is not shown here.

Figure 12 showed that the $R_{\rm AA}$ in the same centrality at RHIC and the LHC show very similar p_T dependence even though the collision systems and center-of-mass energies are vastly different. Figure 18 shows comparisons of $S_{\rm loss}$. Note that the $S_{\rm loss}$ obtained from the ALICE charged hadron measurement is ~30% higher than that from the PHENIX π^0 measurement. This is reasonable considering the fact that the powers (n) in the power-law fit to the p_T spectra are different between the two systems; the power of the PHENIX $p+p$ π^0 s at $\sqrt{s} = 200$ GeV/c is about 8, while that of the ALICE $p+p$ charged hadrons is about 6.

E. Model calculations, transport coefficient

In this section, $R_{\rm AA}$ is compared to four different parton energy loss models, following the method described in Ref. [37]. All four models are incorporated into the same three-dimensional relativistic hydrodynamic calculation with an initial thermalization time $\tau_0 = 0.6$ fm/c and describe the observed elliptic flow, pseudorapidity distributions, and particle spectra at low p_T. The Arnold-Moore-Yaffe formalism (AMY [9,43]) incorporates radiative and collisional energy loss processes in an extended medium in equilibrium at high temperature, i.e., small coupling constant g, where $\alpha_S = \frac{g^2}{4\pi}$. In this approximation, a hierarchy of scales of successively higher powers of the coupling constant can be identified, and it becomes possible to construct an effective theory of soft modes by summing contributions from hard loops into effective propagators and vertices. The higher-twist approach (HT [10]) is based on the medium-enhanced higher-twist corrections to the total cross section in deep inelastic scattering (DIS) off large nuclei [44]. HT incorporates only radiative corrections, but it can directly calculate the medium-modified fragmentation function. The Armesto-Salgado-Wiedemann approach (ASW [11]), which is equivalent to the well-known BDMPS-Z approach [45,46], includes only radiative processes in a medium where the mean free path of the parton is much larger than the color-screening length.

The crucial parameter in all these models is the transport coefficient $\hat{q}$ defined as

$$\hat{q} = \frac{\mu^2}{\lambda}\,(\mathrm{GeV}^2/\mathrm{fm}), \qquad (7)$$

where μ^2 is the average squared transverse momentum transferred from the medium to the parton per collision and λ is the mean free path of the partons. In AMY $\hat{q}$ is directly related to the temperature, while in HT it is related to the local entropy density s ($\propto T^3$) and in ASW it is related to the energy density ε.

Figure 19 compares the measured R_{AA} at two centralities with calculations using the energy loss models described above, incorporated into the same hydrodynamic evolution [37]. In these models, the value of $\hat{q}$ is fixed so as to reproduce the measured R_{AA} in 0–5% centrality collisions. (See Ref. [37] for the definitions of the parameters c_{HG} and K, which can be converted to $\hat{q}_0$.) The values of $\hat{q}_0$ for gluons (defined as the value of $\hat{q}$ at $\tau = 0.6$ fm/c required to describe R_{AA}) differ by a factor of 5: $\hat{q}_0$ is 4.1, 4.3, and 18.5 GeV^2/fm in AMY, HT, and ASW, respectively. The HT formalism was originally developed for deep inelastic scattering off a large nucleus, and hence it has become customary to quote the value of $\hat{q}_0$ for a quark [47], and gives the value $\hat{q}_0 = 1.9$ GeV^2/fm as seen in Fig. 19. Despite the large differences in the values of $\hat{q}$, all models describe both the p_T dependence and the centrality dependence of R_{AA} quite well. Additional experimental constraints are needed to differentiate between the models, for instance, restricting the average path length $\langle L\rangle$ the parton traverses in the medium, which can be achieved not only in two-particle correlation measurements [13] but also by studying $R_{AA}(\Delta\phi)$ of single particles.

F. Nuclear modification factor vs event plane

The overlap region of the colliding nuclei is not azimuthally isotropic, and neither is the medium that is formed in the collision. To first approximation (homogeneous density distribution of nucleons) the overlap region is elliptical, with the short axis being in the reaction plane. As a consequence, the average path length the hard scattered parton traverses in the medium, losing energy in the process, varies with the azimuthal angle $\Delta\phi$, defined experimentally as the relative azimuthal angle between the emerging hadron and the measured event plane. Measuring R_{AA} as a function of $\Delta\phi$ provides additional constraints on the average in-medium path length [14–16], therefore, a more stringent test of energy loss models than the ϕ-integrated R_{AA} alone.

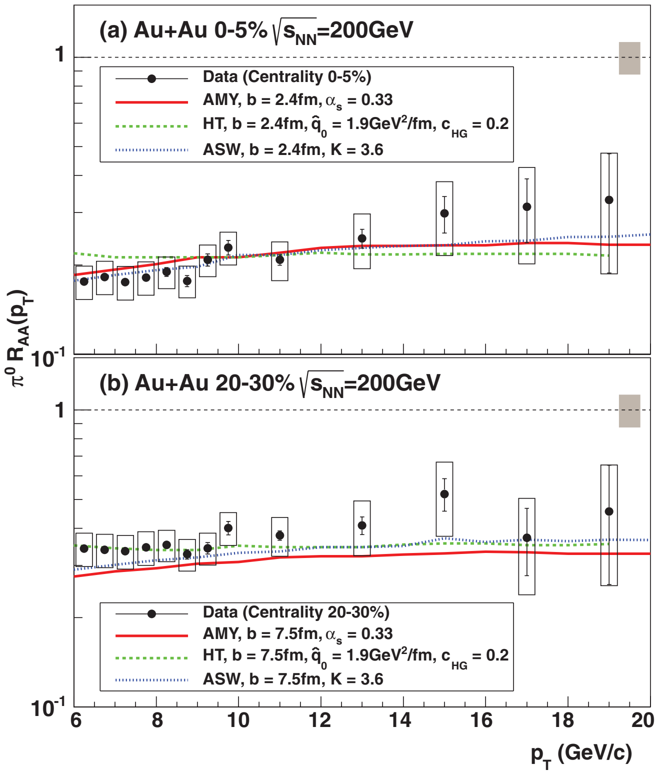

FIG. 19. (Color online) (a) The π^0 R_{AA} as a function of p_T at centrality 0–5%. The solid (red), dashed (green), and dotted (blue) curves are the expectations of the AMY [9,43], HT [10], and ASW [11] models, respectively. (b) The π^0 R_{AA} as a function of p_T at centrality 20–30%. The theoretical curves in both panels are obtained from Ref. [37]. The gray boxes around 1 show global uncertainties and are of type C.

Figure 20 shows the differential nuclear modification factor $R_{AA}(\Delta\phi)$ for six bins in azimuth and six centralities. The participant eccentricities in Table I indicate the difference between the two extremes, in-plane and out-of-plane. In the most-central collisions [panel (a)] the average path lengths in-plane and out-of-plane are almost identical; therefore, the $R_{AA}(\Delta\phi)$ curves almost completely overlap. As one moves to more peripheral collisions, the eccentricity of the overlap region increases and the six curves start to split up showing the expected ordering: suppression is always largest out-of-plane and smallest in-plane. A simple calculation using the participant eccentricity (see Table I) shows that the in-plane path length changes from 6.1 to 3.4 fm when 0–10% and 50–60% centralities are compared, while the out-of-plane path length changes from 6.7 to 5.9 fm between the same two centralities. As a consequence, the out-of-plane $R_{AA}(\Delta\phi)$ changes much less with centrality than the in-plane $R_{AA}(\Delta\phi)$. All these observations are in full agreement with the findings in Ref. [15].

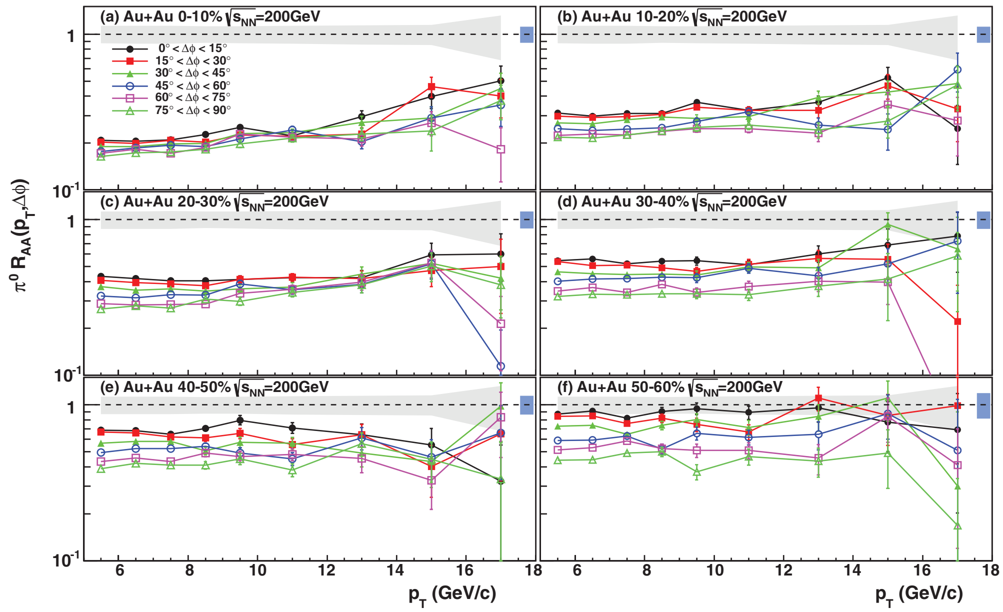

FIG. 20. (Color online) $R_{\mathrm{AA}}(\Delta\phi)$ as a function of p_T for the first six, 10%-wide centrality classes. Each of the six curves represent a 15°-wide bin in azimuth, starting from $\phi = 0°$ (in-plane) up to $\phi = 90°$ (out of plane). The shaded (gray) band around 1 is the systematic uncertainty of the normalizing ϕ-integrated R_{AA}. The shaded (blue) boxes around 1 show global uncertainties and are of type C.

Figure 21 shows the evolution of $R_{\mathrm{AA}}(\Delta\phi)$ with centrality in-plane and out-of-plane (a) at moderate transverse momenta (averaged in the 6–10 GeV/c p_T region) and (b) averaged over all available p_T above 10 GeV/c. As expected, the difference between in-plane and out-of-plane suppression increases with eccentricity (decreasing N_{part}), and the actual values converge toward each other as the centrality increases.

Figure 22 shows the comparisons of the models to the measured in-plane and out-of-plane R_{AA} as a function of p_T for 20–30% centrality. The choice of the 20–30% centrality interval is motivated by the availability of calculations for all the models shown. Furthermore, this interval is a "sweet spot" in determining the reaction plane (minimum uncertainty). While statistical limitations of the reaction-plane-selected R_{AA} vs p_T do not prove that R_{AA} rises with p_T, that rise is apparent from the reaction-plane-integrated measurement shown in Fig. 13. The ϕ (i.e., path length) dependence is clear from the increasing in-plane vs out-of-plane difference in R_{AA} vs centrality and the consistent ordering of the $R_{\mathrm{AA}}(\Delta\phi)$ curves in Fig. 20.

The brackets and bars on the data in Fig. 22 are the statistical uncertainties of the in-plane and out-of-plane R_{AA}. The shaded (gray) band around 1 corresponds to the systematic uncertainty of the average π^0 R_{AA}, while the shaded (blue) boxes at the right end of the $R_{\mathrm{AA}} = 1$ lines show the uncertainty on T_{AA} and are of type C. The shaded bands on the data points are the systematic uncertainty of the $dN/d\phi$ including the uncertainty from the event-plane resolution. Solid (red) circles and solid (blue) squares are the in-plane and out-of-plane R_{AA}, respectively. Panel (a) shows the data overlaid with the AMY calculation [9,43]. While the out-of-plane data are well described, the in-plane data are not, implying that the path-length dependence is too weak in this model. The comparison with HT in panel (b) shows that this model fails to describe both the general trend and the in-plane vs

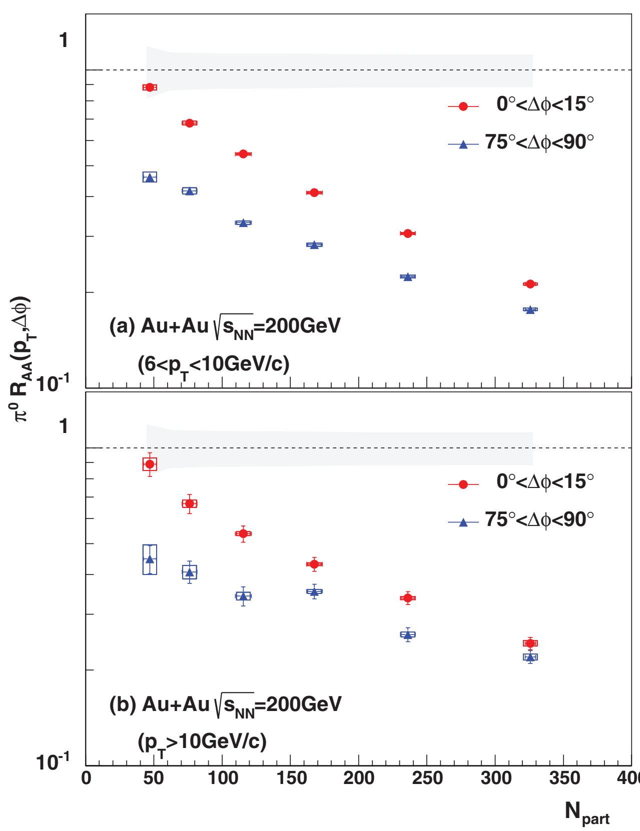

FIG. 21. (Color online) Centrality dependence (expressed in terms of N_{part}) of the π^0 $R_{\mathrm{AA}}(\Delta\phi)$ in-plane solid (red) circles and out-of-plane solid (blue) triangles, averaged (a) in the 6–10 GeV/c transverse momentum region and (b) above 10 GeV/c. Open boxes are systematic uncertainties on $R_{\mathrm{AA}}(\Delta\phi)$.

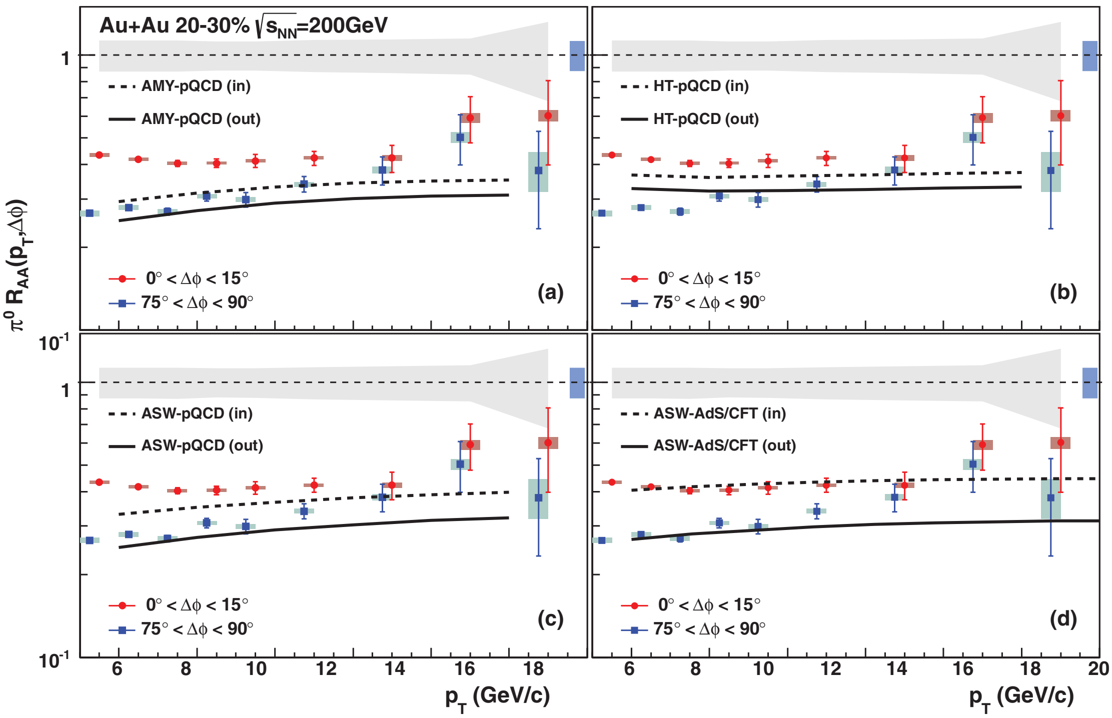

FIG. 22. (Color online) The data points are $R_{AA}(\Delta\phi)$ in 20–30% centrality as a function of p_T for in-plane solid (red) circles and out-of-plane solid (blue) triangles, compared to four model calculations (see text for description and references). (a) pQCD-based AMY [9,43], (b) HT [10], (c) pQCD-based ASW [11], and (d) ASW using AdS/CFT correspondence [12]. The curves in panels (a)–(c) are taken from Ref. [37]. The dashed and solid lines are the in-plane and out-of-plane predictions, respectively. The definitions of the bands and boxes are the same as those in Fig. 20.

out-of-plane differences. The ASW formalism [panel (c)] describes the out-of-plane suppression as well as AMY and shows a somewhat larger in-plane vs out-of-plane difference, but is still inconsistent with the data. It should be noted that in these three models the energy loss is proportional to L^2, where L is the path length in the medium, and the quadratic dependence is characteristic when radiative energy loss is the dominant mechanism.

Finally, in Fig. 22(d) the data are compared to a model that invokes strong coupling in the medium via an anti-de-Sitter space/conformal field theory (AdS/CFT)-inspired model. The ASW-AdS/CFT formalism [12] incorporates the ASW treatment of hard processes, but for the soft processes assumes strong coupling. Such a hybrid procedure was first suggested in Ref. [48]. The virtual gluons radiated into the medium are governed by pQCD, but the interactions of those virtual gluons with the medium to bring them on shell is done by assuming that the transverse momentum squared is proportional to L^2 as given by an AdS/CFT calculation [12,49]. This is in contrast to the weak-coupling expression for the transverse momentum squared, $\hat{q}L$. This results in an energy loss proportional to L^3 instead of L^2 as in the case of the pQCD-based models. Figure 22(d) shows that the ASW-AdS/CFT model describes both the general shape and the absolute difference of the in-plane and out-of-plane data well. The observation that models with path-length dependence of energy loss stronger than L^2 are in better agreement with the measurements is consistent with the findings in Ref. [16].

IV. SUMMARY AND CONCLUSIONS

In summary, the large data set presented in this paper made possible a measurement of the π^0 invariant yield in $\sqrt{s_{NN}} =$ 200 GeV Au + Au collisions up to 20 GeV/c transverse momentum. This has led to a precision measurement of the η/π^0 ratio in Au + Au collisions, which is constant as a function of both centrality and p_T, $\eta/\pi^0 = 0.45 \pm 0.01(\text{stat}) \pm 0.04(\text{syst})$, and consistent with the values observed in dAu and $p + p$. The large observed π^0 suppression is fully consistent with earlier findings, and a slow but significant rise of R_{AA} vs p_T with a slope of $0.0106^{+0.0034}_{-0.0029}$ $(\text{GeV}/c)^{-1}$ for central collisions is now observed for the first time at RHIC energies. This has been an expectation of all pQCD-based parton energy loss models. The large data set has also made possible the calculation of a phenomenological $\Delta E/E$ energy loss. The differential $R_{AA}(\Delta\phi)$, testing the path-length dependence of energy loss, is measured up to p_T of 20 GeV/c and is compared to various energy loss calculations. While all models considered describe the ϕ-integrated R_{AA} adequately, the pQCD-based calculations where the energy loss depends on the path length as L^2 fail to describe the differential $R_{AA}(\Delta\phi)$. The data require an energy loss with a power greater than 2, as given by models in which the soft interactions with the medium are strongly coupled.

These findings are consistent with the conclusions of Ref. [16] in which data on the elliptic flow of high-p_T (>6 GeV) π^0s is shown to be inconsistent with pQCD-based models. To explore the strong coupling regime, a comparison was made to the same ASW-AdS/CFT model used in this work, as well as to a phenomenological model [50] in which the energy loss was proportional to L^3, both of which were able to fit the data. Both the current measurement and Ref. [16] explore a region of high p_T where the mechanism leading to an azimuthally anisotropic yield is parton energy loss rather than hydrodynamical flow. It is increasingly difficult for purely pQCD-based models to explain these results and one is led to the tentative conclusion that strong coupling plays an important role in parton energy loss in the medium. At present, the best method to do the relevant calculations is in an AdS/CFT framework. Similar conclusions are reached when one looks at the behavior of heavy quarks [51], where higher quality data will soon be available. Recent preliminary results on the suppression pattern seen at the LHC for $p_T >$ 6 GeV/c are strikingly similar to those seen at RHIC. In this paper, a phenomenological calculation of fractional energy loss is given, which indicates that the energy loss at the LHC (ALICE data) is about 30% higher than that at RHIC and that the loss falls slightly with energy. The dependence of these observables on momentum and center-of-mass energy (presumably on energy density) will be a crucial factor in untangling the underlying mechanisms of parton energy loss.

Recently, experiments at the LHC have begun to examine the behavior of fully reconstructed jets, which should give more easily interpretable information on this phenomenon. Future work at both the LHC and RHIC should bring data on path-length dependence of fully reconstructed jets, jet widths, and heavy-quark jets which will add a wealth of new information. In addition, a more complete understanding of the initial state is also needed both for the initial configuration of hydrodynamical models and as a calibration of the hard probes that are used in these measurements.

ACKNOWLEDGMENTS

We thank the staff of the Collider-Accelerator and Physics Departments at Brookhaven National Laboratory and the staff of the other PHENIX participating institutions for their vital contributions. We acknowledge support from the Office of Nuclear Physics in the Office of Science of the Department of Energy; the National Science Foundation; the Abilene Christian University Research Council; the Research Foundation of SUNY; the Dean of the College of Arts and Sciences, Vanderbilt University (USA); the Ministry of Education, Culture, Sports, Science, and Technology and the Japan Society for the Promotion of Science (Japan); Conselho Nacional de Desenvolvimento Científico e Tecnológico and Fundação de Amparo à Pesquisa do Estado de São Paulo (Brazil); the Natural Science Foundation of China (People's Republic of China); the Ministry of Education, Youth and Sports (Czech Republic); the Centre National de la Recherche Scientifique, the Commissariat à l'Énergie Atomique, and the Institut National de Physique Nucléaire et de Physique des Particules (France); the Bundesministerium für Bildung und Forschung, Deutscher Akademischer Austausch Dienst, and Alexander von Humboldt Stiftung (Germany); the Hungarian National Science Fund, OTKA (Hungary); the Department of Atomic Energy and Department of Science and Technology (India); the Israel Science Foundation (Israel); the National Research Foundation and WCU Program of the Ministry Education Science and Technology (Korea); the Ministry of Education and Science, Russian Academy of Sciences, Federal Agency of Atomic Energy (Russia); VR and the Wallenberg Foundation (Sweden); the US Civilian Research and Development Foundation for the Independent States of the Former Soviet Union; the US-Hungarian Fulbright Foundation for Educational Exchange; and the US-Israel Binational Science Foundation.

APPENDIX

Tables V and VI give values for the invariant yields for neutral pions, as shown in Fig. 5. Tables VII and VIII give values of R_{AA} for neutral pions, as shown in Figs. 11 and 12, respectively.

TABLE V. Invariant yields of neutral pions as a function of p_T at $|y| < 0.35$ in Au + Au collisions at $\sqrt{s_{NN}} = 200$ GeV for the very-most-central 0–5% centrality. Syst. (B) refers to type-B systematic errors. See Fig. 5.

Centrality	p_T	Inv. yield	Stat. error	Fraction %	Syst. (B) error	Fraction %
0–5%	5.25	9.394×10^{-5}	8.7×10^{-7}	0.92	8.4×10^{-6}	8.9
	5.75	4.524×10^{-5}	5.2×10^{-7}	1.1	4.0×10^{-6}	8.9
	6.25	2.273×10^{-5}	3.2×10^{-7}	1.4	2.0×10^{-6}	8.9
	6.75	1.253×10^{-5}	2.2×10^{-7}	1.7	1.1×10^{-6}	8.9
	7.25	6.862×10^{-6}	1.5×10^{-7}	2.1	6.1×10^{-7}	8.9
	7.75	4.164×10^{-6}	1.1×10^{-7}	2.5	3.7×10^{-7}	8.9
	8.25	2.598×10^{-6}	7.8×10^{-8}	3.0	2.0×10^{-7}	7.6
	8.75	1.545×10^{-6}	5.8×10^{-8}	3.7	1.2×10^{-7}	7.6
	9.25	1.118×10^{-6}	4.5×10^{-8}	4.0	8.6×10^{-8}	7.7
	9.75	7.684×10^{-7}	3.5×10^{-8}	4.6	6.3×10^{-8}	8.2
	11	2.837×10^{-7}	9.6×10^{-9}	3.4	3.1×10^{-8}	11
	13	8.685×10^{-8}	4.9×10^{-9}	5.7	1.5×10^{-8}	18
	15	2.659×10^{-8}	3.0×10^{-9}	11	6.7×10^{-9}	25
	17	9.547×10^{-9}	1.9×10^{-9}	20	3.1×10^{-9}	33
	19	4.450×10^{-9}	1.7×10^{-9}	38	1.8×10^{-9}	41

TABLE VI. Invariant yields of neutral pions as a function of p_T at $|y| < 0.35$ in Au + Au collisions at $\sqrt{s_{NN}} = 200$ GeV for the indicated centrality ranges, including minimum bias (0–93%). Syst. (B) refers to type-B systematic errors. See Fig. 5.

Centrality	p_T	Inv. yield	Stat. error	Fraction %	Syst. (B) error	Fraction %	Centrality	p_T	Inv. yield	Stat. error	Fraction %	Syst. (B) error	Fraction %
0–10%	5.25	8.969×10^{-5}	5.6×10^{-7}	0.63	8.0×10^{-6}	8.9	50–60%	5.25	2.147×10^{-5}	1.8×10^{-7}	0.84	1.9×10^{-6}	8.9
	5.75	4.309×10^{-5}	3.4×10^{-7}	0.79	3.8×10^{-6}	8.9		5.75	1.007×10^{-5}	1.2×10^{-7}	1.1	9.0×10^{-7}	8.9
	6.25	2.193×10^{-5}	2.2×10^{-7}	0.99	2.0×10^{-6}	8.9		6.25	5.253×10^{-6}	7.9×10^{-8}	1.5	4.7×10^{-7}	8.9
	6.75	1.190×10^{-5}	1.4×10^{-7}	1.2	1.1×10^{-6}	8.9		6.75	2.785×10^{-6}	5.4×10^{-8}	1.9	2.5×10^{-7}	8.9
	7.25	6.738×10^{-6}	1.0×10^{-7}	1.5	6.0×10^{-7}	8.9		7.25	1.535×10^{-6}	3.9×10^{-8}	2.5	1.4×10^{-7}	8.9
	7.75	4.063×10^{-6}	7.2×10^{-8}	1.8	3.6×10^{-7}	8.9		7.75	9.018×10^{-7}	2.8×10^{-8}	3.2	8.0×10^{-8}	8.9
	8.25	2.457×10^{-6}	5.3×10^{-8}	2.2	1.9×10^{-7}	7.6		8.25	5.628×10^{-7}	2.2×10^{-8}	3.9	4.3×10^{-8}	7.6
	8.75	1.551×10^{-6}	4.0×10^{-8}	2.6	1.2×10^{-7}	7.6		8.75	3.352×10^{-7}	1.6×10^{-8}	4.9	2.6×10^{-8}	7.6
	9.25	1.085×10^{-6}	3.1×10^{-8}	2.9	8.4×10^{-8}	7.7		9.25	2.041×10^{-7}	1.3×10^{-8}	6.2	1.6×10^{-8}	7.7
	9.75	6.798×10^{-7}	2.4×10^{-8}	3.5	5.6×10^{-8}	8.2		9.75	1.459×10^{-7}	1.0×10^{-8}	6.8	1.2×10^{-8}	8.2
	11	2.767×10^{-7}	6.7×10^{-9}	2.4	3.1×10^{-8}	11		11	5.270×10^{-8}	2.8×10^{-9}	5.3	5.8×10^{-9}	11
	13	7.651×10^{-8}	3.3×10^{-9}	4.3	1.4×10^{-8}	18		13	1.563×10^{-8}	1.7×10^{-9}	11	2.8×10^{-9}	18
	15	2.603×10^{-8}	2.0×10^{-9}	7.9	6.6×10^{-9}	25		15	4.387×10^{-9}	7.8×10^{-10}	18	1.1×10^{-9}	25
	17	1.031×10^{-8}	1.4×10^{-9}	14	3.4×10^{-9}	33		17	9.288×10^{-10}	4.2×10^{-10}	45	3.1×10^{-10}	33
	19	3.194×10^{-9}	1.0×10^{-9}	32	1.3×10^{-9}	41		19	3.030×10^{-10}	3.0×10^{-10}	100	1.2×10^{-10}	41
10–20%	5.25	8.053×10^{-5}	4.6×10^{-7}	0.57	7.2×10^{-6}	8.9	60–70%	5.25	1.155×10^{-5}	1.3×10^{-7}	1.1	1.0×10^{-6}	8.9
	5.75	3.806×10^{-5}	2.8×10^{-7}	0.74	3.4×10^{-6}	8.9		5.75	5.650×10^{-6}	8.4×10^{-8}	1.5	5.0×10^{-7}	8.9
	6.25	1.882×10^{-5}	1.8×10^{-7}	0.96	1.7×10^{-6}	8.9		6.25	2.759×10^{-6}	5.7×10^{-8}	2.1	2.5×10^{-7}	8.9
	6.75	1.031×10^{-5}	1.2×10^{-7}	1.2	9.2×10^{-7}	8.9		6.75	1.587×10^{-6}	4.0×10^{-8}	2.6	1.4×10^{-7}	8.9
	7.25	5.924×10^{-6}	8.7×10^{-8}	1.5	5.3×10^{-7}	8.9		7.25	8.197×10^{-7}	2.8×10^{-8}	3.4	7.3×10^{-8}	8.9
	7.75	3.469×10^{-6}	6.2×10^{-8}	1.8	3.1×10^{-7}	8.9		7.75	4.848×10^{-7}	2.1×10^{-8}	4.3	4.3×10^{-8}	8.9
	8.25	2.161×10^{-6}	4.7×10^{-8}	2.2	1.7×10^{-7}	7.6		8.25	2.964×10^{-7}	1.6×10^{-8}	5.2	2.3×10^{-8}	7.6
	8.75	1.345×10^{-6}	3.5×10^{-8}	2.6	1.0×10^{-7}	7.6		8.75	1.863×10^{-7}	1.2×10^{-8}	6.5	1.4×10^{-8}	7.6
	9.25	8.844×10^{-7}	2.7×10^{-8}	3.1	6.8×10^{-8}	7.7		9.25	1.011×10^{-7}	9.1×10^{-9}	9.0	7.8×10^{-9}	7.7
	9.75	5.838×10^{-7}	2.1×10^{-8}	3.6	4.8×10^{-8}	8.2		9.75	8.904×10^{-8}	8.1×10^{-9}	9.1	7.3×10^{-9}	8.2
	11	2.300×10^{-7}	5.9×10^{-9}	2.6	2.5×10^{-8}	11		11	2.715×10^{-8}	2.0×10^{-9}	7.3	3.0×10^{-9}	11
	13	6.141×10^{-8}	2.9×10^{-9}	4.7	1.1×10^{-8}	18		13	9.210×10^{-9}	1.1×10^{-9}	11	1.6×10^{-9}	18
	15	1.971×10^{-8}	1.7×10^{-9}	8.8	5.0×10^{-9}	25		15	3.129×10^{-9}	6.5×10^{-10}	21	7.9×10^{-10}	25
	17	6.953×10^{-9}	1.3×10^{-9}	18	2.3×10^{-9}	33		17	2.029×10^{-9}	6.1×10^{-10}	30	6.7×10^{-10}	33
	19	2.490×10^{-9}	8.8×10^{-10}	35	1.0×10^{-9}	41		19	3.015×10^{-10}	3.0×10^{-10}	100	1.2×10^{-10}	41
20–30%	5.25	6.693×10^{-5}	3.8×10^{-7}	0.57	6.0×10^{-6}	8.9	70–80%	5.25	5.486×10^{-6}	8.7×10^{-8}	1.6	4.9×10^{-7}	8.9
	5.75	3.084×10^{-5}	2.3×10^{-7}	0.76	2.8×10^{-6}	8.9		5.75	2.651×10^{-6}	5.7×10^{-8}	2.2	2.4×10^{-7}	8.9
	6.25	1.563×10^{-5}	1.5×10^{-7}	0.98	1.4×10^{-6}	8.9		6.25	1.330×10^{-6}	3.9×10^{-8}	2.9	1.2×10^{-7}	8.9
	6.75	8.231×10^{-6}	1.0×10^{-7}	1.3	7.3×10^{-7}	8.9		6.75	6.962×10^{-7}	2.6×10^{-8}	3.8	6.2×10^{-8}	8.9
	7.25	4.649×10^{-6}	7.3×10^{-8}	1.6	4.1×10^{-7}	8.9		7.25	4.293×10^{-7}	2.0×10^{-8}	4.7	3.8×10^{-8}	8.9
	7.75	2.797×10^{-6}	5.4×10^{-8}	1.9	2.5×10^{-7}	8.9		7.75	2.404×10^{-7}	1.5×10^{-8}	6.4	2.1×10^{-8}	8.9
	8.25	1.705×10^{-6}	4.0×10^{-8}	2.3	1.3×10^{-7}	7.6		8.25	1.424×10^{-7}	1.1×10^{-8}	7.6	1.1×10^{-8}	7.6
	8.75	1.012×10^{-6}	3.0×10^{-8}	2.9	7.7×10^{-8}	7.6		8.75	9.797×10^{-8}	8.3×10^{-9}	8.4	7.5×10^{-9}	7.6
	9.25	6.519×10^{-7}	2.3×10^{-8}	3.5	5.0×10^{-8}	7.7		9.25	5.629×10^{-8}	6.6×10^{-9}	12	4.3×10^{-9}	7.7
	9.75	4.762×10^{-7}	1.8×10^{-8}	3.9	3.9×10^{-8}	8.2		9.75	4.044×10^{-8}	5.0×10^{-9}	12	3.3×10^{-9}	8.2
	11	1.826×10^{-7}	5.2×10^{-9}	2.9	2.0×10^{-8}	11		11	1.212×10^{-8}	1.2×10^{-9}	10	1.3×10^{-9}	11
	13	5.116×10^{-8}	2.6×10^{-9}	5.1	9.1×10^{-9}	18		13	4.448×10^{-9}	7.3×10^{-10}	16	7.9×10^{-10}	18
	15	1.646×10^{-8}	1.6×10^{-9}	9.5	4.1×10^{-9}	25		15	6.762×10^{-9}	3.0×10^{-10}	45	1.7×10^{-10}	25
	17	3.999×10^{-9}	8.7×10^{-10}	22	1.3×10^{-9}	33		17	3.663×10^{-9}	2.6×10^{-10}	71	1.2×10^{-10}	33
	19	2.166×10^{-9}	8.2×10^{-10}	38	8.8×10^{-10}	41		19	–	–	–	–	–
30–40%	5.25	4.960×10^{-5}	3.0×10^{-7}	0.61	4.4×10^{-6}	8.9	80–93%	5.25	1.748×10^{-6}	4.3×10^{-8}	2.5	1.6×10^{-7}	8.9
	5.75	2.294×10^{-5}	1.9×10^{-7}	0.83	2.0×10^{-6}	8.9		5.75	8.505×10^{-7}	2.8×10^{-8}	3.3	7.6×10^{-8}	8.9
	6.25	1.194×10^{-5}	1.3×10^{-7}	1.1	1.1×10^{-6}	8.9		6.25	4.344×10^{-7}	2.0×10^{-8}	4.5	3.9×10^{-8}	8.9
	6.75	6.265×10^{-6}	8.7×10^{-8}	1.4	5.6×10^{-7}	8.9		6.75	2.451×10^{-7}	1.4×10^{-8}	5.5	2.2×10^{-8}	8.9
	7.25	3.449×10^{-6}	6.1×10^{-8}	1.8	3.1×10^{-7}	8.9		7.25	1.460×10^{-7}	1.0×10^{-8}	7.0	1.3×10^{-8}	8.9
	7.75	2.119×10^{-6}	4.5×10^{-8}	2.1	1.9×10^{-7}	8.9		7.75	7.727×10^{-8}	7.2×10^{-9}	9.4	6.9×10^{-9}	8.9
	8.25	1.266×10^{-6}	3.3×10^{-8}	2.6	9.7×10^{-8}	7.6		8.25	4.874×10^{-8}	5.6×10^{-9}	12	3.7×10^{-9}	7.6
	8.75	7.920×10^{-7}	2.5×10^{-8}	3.2	6.1×10^{-8}	7.6		8.75	2.374×10^{-8}	4.4×10^{-9}	19	1.8×10^{-9}	7.6
	9.25	4.733×10^{-7}	1.9×10^{-8}	4.0	3.7×10^{-8}	7.7		9.25	1.599×10^{-8}	2.8×10^{-9}	18	1.2×10^{-9}	7.7
	9.75	3.024×10^{-7}	1.5×10^{-8}	4.8	2.5×10^{-8}	8.2		9.75	8.472×10^{-9}	2.0×10^{-9}	24	7.0×10^{-10}	8.2
	11	1.297×10^{-7}	4.3×10^{-9}	3.3	1.4×10^{-8}	11		11	5.041×10^{-9}	7.0×10^{-10}	14	5.6×10^{-10}	11
	13	3.537×10^{-8}	2.2×10^{-9}	6.1	6.3×10^{-9}	18		13	9.230×10^{-10}	2.9×10^{-10}	32	1.6×10^{-10}	18
	15	1.117×10^{-8}	1.5×10^{-9}	13	2.8×10^{-9}	25		15	1.038×10^{-10}	1.0×10^{-10}	100	2.6×10^{-11}	25
	17	3.195×10^{-9}	7.7×10^{-10}	24	1.1×10^{-9}	33		17	1.407×10^{-10}	1.4×10^{-10}	100	4.6×10^{-11}	33
	19	1.531×10^{-9}	6.8×10^{-10}	45	6.2×10^{-10}	41		19	–	–	–	–	–
40–50%	5.25	3.395×10^{-5}	2.3×10^{-7}	0.69	3.0×10^{-6}	8.9	0–93%	5.25	4.038×10^{-5}	1.0×10^{-7}	0.26	3.6×10^{-6}	8.9
	5.75	1.612×10^{-5}	1.5×10^{-7}	0.93	1.4×10^{-6}	8.9		5.75	1.880×10^{-5}	6.3×10^{-8}	0.33	1.7×10^{-6}	8.9
	6.25	8.369×10^{-6}	1.0×10^{-7}	1.2	7.5×10^{-7}	8.9		6.25	9.464×10^{-6}	4.1×10^{-8}	0.43	8.4×10^{-7}	8.9

TABLE VI. *(Continued.)*

Centrality	p_T	Inv. yield	Stat. error	Fraction %	Syst. (B) error	Fraction %	Centrality	p_T	Inv. yield	Stat. error	Fraction %	Syst. (B) error	Fraction %
	6.75	4.444×10^{-6}	7.0×10^{-8}	1.6	4.0×10^{-7}	8.9		6.75	5.047×10^{-6}	2.7×10^{-8}	0.54	4.5×10^{-7}	8.9
	7.25	2.397×10^{-6}	5.0×10^{-8}	2.1	2.1×10^{-7}	8.9		7.25	2.821×10^{-6}	1.9×10^{-8}	0.68	2.5×10^{-7}	8.9
	7.75	1.492×10^{-6}	3.7×10^{-8}	2.5	1.3×10^{-7}	8.9		7.75	1.688×10^{-6}	1.4×10^{-8}	0.83	1.5×10^{-7}	8.9
	8.25	8.663×10^{-7}	2.7×10^{-8}	3.1	6.6×10^{-8}	7.6		8.25	1.022×10^{-6}	1.0×10^{-8}	1.0	7.8×10^{-8}	7.6
	8.75	5.578×10^{-7}	2.1×10^{-8}	3.7	4.3×10^{-8}	7.6		8.75	6.311×10^{-7}	7.8×10^{-9}	1.2	4.8×10^{-8}	7.6
	9.25	3.434×10^{-7}	1.6×10^{-8}	4.5	2.6×10^{-8}	7.7		9.25	4.075×10^{-7}	6.0×10^{-9}	1.5	3.1×10^{-8}	7.7
	9.75	2.377×10^{-7}	1.3×10^{-8}	5.3	2.0×10^{-8}	8.2		9.75	2.744×10^{-7}	4.7×10^{-9}	1.7	2.3×10^{-8}	8.2
	11	8.341×10^{-8}	3.5×10^{-9}	4.2	9.2×10^{-9}	11		11	1.073×10^{-7}	1.3×10^{-9}	1.2	1.2×10^{-8}	11
	13	2.352×10^{-8}	1.8×10^{-9}	7.7	4.2×10^{-9}	18		13	2.968×10^{-8}	6.6×10^{-10}	2.2	5.3×10^{-9}	18
	15	4.544×10^{-9}	2.6×10^{-9}	56	1.1×10^{-9}	25		15	9.454×10^{-9}	4.0×10^{-10}	4.2	2.4×10^{-9}	25
	17	2.233×10^{-9}	6.4×10^{-10}	29	7.3×10^{-10}	33		17	3.208×10^{-9}	2.6×10^{-10}	8.1	1.1×10^{-9}	33
	19	1.517×10^{-9}	6.8×10^{-10}	45	6.2×10^{-10}	41		19	1.224×10^{-9}	2.0×10^{-10}	16	5.0×10^{-10}	41

TABLE VII. Nuclear modification factors, R_{AA}, for neutral pions as a function of p_T at $|y| < 0.35$ in Au + Au collisions at $\sqrt{s_{NN}} = 200$ GeV for the indicated centrality ranges, including minimum bias (0–93%). Syst. (B) refers to type-B systematic errors. The global systematic uncertainties (type C) are $p + p$ normalization (9.7%) and off-vertex (1.5%). See Fig. 11.

Centrality	p_T	R_{AA}	Stat. error	Fraction %	Syst. (B) error	Fraction %	Centrality	p_T	R_{AA}	Stat. error	Fraction %	Syst. (B) error	Fraction %
0–10%	5.25	0.1859	0.0014	0.74	0.024	13	50–60%	5.25	0.6691	0.0062	0.92	0.086	13
	5.75	0.1855	0.0018	0.95	0.024	13		5.75	0.6517	0.0082	1.3	0.084	13
	6.25	0.1882	0.0023	1.2	0.024	13		6.25	0.6776	0.011	1.7	0.087	13
	6.75	0.1922	0.0029	1.5	0.025	13		6.75	0.6765	0.015	2.2	0.087	13
	7.25	0.1908	0.0036	1.9	0.025	13		7.25	0.6533	0.018	2.8	0.084	13
	7.75	0.1967	0.0045	2.3	0.025	13		7.75	0.6562	0.023	3.5	0.085	13
	8.25	0.1990	0.0056	2.8	0.024	12		8.25	0.6851	0.030	4.3	0.083	12
	8.75	0.1970	0.0066	3.4	0.024	12		8.75	0.6399	0.034	5.4	0.078	12
	9.25	0.2241	0.0089	4.0	0.028	12		9.25	0.6339	0.043	6.8	0.078	12
	9.75	0.2250	0.011	4.9	0.028	13		9.75	0.7255	0.055	7.6	0.092	13
	11	0.2253	0.0077	3.4	0.034	15		11	0.6448	0.038	5.9	0.096	15
	13	0.2403	0.015	6.3	0.050	21		13	0.7378	0.085	12	0.15	21
	15	0.3244	0.037	11	0.091	28		15	0.8217	0.16	19	0.23	28
	17	0.3763	0.072	19	0.13	36		17	0.5097	0.24	47	0.18	36
	19	0.2639	0.10	38	0.12	44		19	0.3762	0.38	100	0.16	44
10–20%	5.25	0.2630	0.0018	0.69	0.034	13	60–70%	5.25	0.7726	0.0091	1.2	0.099	13
	5.75	0.2581	0.0023	0.91	0.033	13		5.75	0.7851	0.012	1.6	0.10	13
	6.25	0.2545	0.0030	1.2	0.033	13		6.25	0.7642	0.017	2.2	0.098	13
	6.75	0.2625	0.0040	1.5	0.034	13		6.75	0.8278	0.022	2.7	0.11	13
	7.25	0.2643	0.0050	1.9	0.034	13		7.25	0.7490	0.027	3.6	0.097	13
	7.75	0.2646	0.0061	2.3	0.034	13		7.75	0.7576	0.034	4.5	0.098	13
	8.25	0.2757	0.0078	2.8	0.034	12		8.25	0.7747	0.043	5.5	0.094	12
	8.75	0.2691	0.0091	3.4	0.033	12		8.75	0.7636	0.053	6.9	0.093	12
	9.25	0.2879	0.012	4.1	0.035	12		9.25	0.6745	0.064	9.4	0.083	12
	9.75	0.3043	0.015	5.0	0.038	13		9.75	0.9509	0.092	9.7	0.12	13
	11	0.2950	0.010	3.5	0.044	15		11	0.7135	0.055	7.7	0.11	15
	13	0.3038	0.020	6.6	0.063	21		13	0.9334	0.12	12	0.19	21
	15	0.3870	0.046	12	0.11	28		15	1.259	0.28	22	0.35	28
	17	0.4000	0.089	22	0.14	36		17	2.391	0.79	33	0.85	36
	19	0.3240	0.13	41	0.14	44		19	0.8040	0.82	100	0.35	44
20–30%	5.25	0.3528	0.0024	0.69	0.045	13	70–80%	5.25	0.8701	0.014	1.6	0.11	13
	5.75	0.3377	0.0031	0.92	0.043	13		5.75	0.8731	0.019	2.2	0.11	13
	6.25	0.3412	0.0041	1.2	0.044	13		6.25	0.8736	0.026	3.0	0.11	13
	6.75	0.3382	0.0053	1.6	0.044	13		6.75	0.8608	0.034	3.9	0.11	13
	7.25	0.3347	0.0065	2.0	0.043	13		7.25	0.9298	0.045	4.9	0.12	13
	7.75	0.3444	0.0083	2.4	0.045	13		7.75	0.8904	0.059	6.6	0.12	13
	8.25	0.3511	0.010	3.0	0.043	12		8.25	0.8823	0.069	7.8	0.11	12
	8.75	0.3268	0.012	3.6	0.040	12		8.75	0.9520	0.083	8.7	0.12	12
	9.25	0.3425	0.015	4.4	0.042	12		9.25	0.8898	0.11	12	0.11	12
	9.75	0.4006	0.021	5.1	0.051	13		9.75	1.024	0.13	13	0.13	13

TABLE VII. *(Continued.)*

Centrality	p_T	R_{AA}	Stat. error	Fraction %	Syst. (B) error	Fraction %	Centrality	p_T	R_{AA}	Stat. error	Fraction %	Syst. (B) error	Fraction %
	11	0.3779	0.014	3.7	0.057	15		11	0.7552	0.079	10	0.11	15
	13	0.4085	0.028	6.9	0.085	21		13	1.069	0.18	17	0.22	21
	15	0.5216	0.065	12	0.15	28		15	0.6448	0.29	45	0.18	28
	17	0.3713	0.095	26	0.13	36		17	1.023	0.74	72	0.37	36
	19	0.4550	0.20	43	0.20	44		19	–	–	–	–	–
30–40%	5.25	0.4408	0.0032	0.72	0.056	13	80–93%	5.25	0.8298	0.021	2.5	0.11	13
	5.75	0.4234	0.0041	0.98	0.054	13		5.75	0.8385	0.028	3.4	0.11	13
	6.25	0.4394	0.0056	1.3	0.056	13		6.25	0.8537	0.039	4.6	0.11	13
	6.75	0.4341	0.0072	1.7	0.056	13		6.75	0.9070	0.051	5.6	0.12	13
	7.25	0.4186	0.0089	2.1	0.054	13		7.25	0.9464	0.067	7.1	0.12	13
	7.75	0.4398	0.011	2.6	0.057	13		7.75	0.8566	0.081	9.5	0.11	13
	8.25	0.4397	0.014	3.2	0.053	12		8.25	0.9038	0.11	12	0.11	12
	8.75	0.4313	0.017	3.9	0.053	12		8.75	0.6904	0.13	19	0.084	12
	9.25	0.4193	0.020	4.9	0.052	12		9.25	0.7566	0.14	18	0.093	12
	9.75	0.4291	0.025	5.9	0.054	13		9.75	0.6419	0.15	24	0.081	13
	11	0.4526	0.019	4.1	0.068	15		11	0.9396	0.13	14	0.14	15
	13	0.4762	0.036	7.6	0.099	21		13	0.6637	0.21	32	0.14	21
	15	0.5969	0.092	15	0.17	28		15	0.2963	0.30	100	0.083	28
	17	0.5002	0.14	28	0.18	36		17	1.176	1.2	100	0.42	36
	19	0.5423	0.27	49	0.24	44		19	–	–	–	–	–
40–50%	5.25	0.5422	0.0043	0.79	0.069	13	0–93%	5.25	0.3105	0.0014	0.46	0.040	13
	5.75	0.5346	0.0057	1.1	0.069	13		5.75	0.3002	0.0019	0.62	0.038	13
	6.25	0.5532	0.0078	1.4	0.071	13		6.25	0.3013	0.0025	0.82	0.039	13
	6.75	0.5531	0.010	1.8	0.071	13		6.75	0.3025	0.0032	1.1	0.039	13
	7.25	0.5227	0.012	2.4	0.067	13		7.25	0.2962	0.0040	1.4	0.038	13
	7.75	0.5562	0.016	2.9	0.072	13		7.75	0.3031	0.0051	1.7	0.039	13
	8.25	0.5404	0.020	3.6	0.066	12		8.25	0.3070	0.0064	2.1	0.037	12
	8.75	0.5457	0.024	4.3	0.067	12		8.75	0.2973	0.0074	2.5	0.036	12
	9.25	0.5466	0.029	5.3	0.067	12		9.25	0.3123	0.0096	3.1	0.038	12
	9.75	0.6059	0.038	6.3	0.077	13		9.75	0.3368	0.013	3.8	0.043	13
	11	0.5231	0.025	4.8	0.078	15		11	0.3240	0.0088	2.7	0.048	15
	13	0.5690	0.051	9.0	0.12	21		13	0.3458	0.018	5.1	0.072	21
	15	0.4362	0.25	57	0.12	28		15	0.4370	0.040	9.2	0.12	28
	17	0.6280	0.20	32	0.22	36		17	0.4344	0.067	16	0.16	36
	19	0.9655	0.48	49	0.42	44		19	0.3750	0.10	27	0.16	44

TABLE VIII. Nuclear modification factors, R_{AA}, for neutral pions as a function of p_T at $|y| < 0.35$ in Au + Au collisions at $\sqrt{s_{NN}} = 200$ GeV for the very-most-central 0–5% collisions. Syst. (B) refers to type-B systematic errors. The global systematic uncertainties (type C) are $p + p$ normalization (9.7%) and off-vertex (1.5%). See Fig. 12.

Centrality	p_T	R_{AA}	Stat. error	Fraction %	Syst. (B) error	Fraction %
0–5%	5.25	0.1753	0.0018	1.0	0.022	13
	5.75	0.1753	0.0022	1.3	0.022	13
	6.25	0.1756	0.0028	1.6	0.023	13
	6.75	0.1823	0.0036	2.0	0.023	13
	7.25	0.1749	0.0043	2.4	0.023	13
	7.75	0.1815	0.0053	2.9	0.023	13
	8.25	0.1894	0.0067	3.5	0.023	12
	8.75	0.1766	0.0076	4.3	0.022	12
	9.25	0.2080	0.010	4.8	0.026	12
	9.75	0.2288	0.013	5.7	0.029	13
	11	0.2079	0.0087	4.2	0.031	15
	13	0.2455	0.018	7.3	0.051	21
	15	0.2982	0.042	14	0.083	28
	17	0.3137	0.076	24	0.11	36
	19	0.3308	0.14	43	0.14	44

[1] K. Adcox *et al*. (PHENIX Collaboration), Phys. Rev. Lett. **88**, 022301 (2001).
[2] S. S. Adler *et al*. (PHENIX Collaboration), Phys. Rev. Lett. **91**, 072301 (2003).
[3] J. Adams *et al*. (STAR Collaboration), Phys. Rev. Lett. **91**, 172302 (2003).
[4] S. S. Adler *et al*. (PHENIX Collaboration), Phys. Rev. Lett. **91**, 072303 (2003).
[5] J. D. Bjorken, Fermilab-Pub-82/59-THY, 1982.
[6] X.-N. Wang and M. Gyulassy, Phys. Rev. Lett. **68**, 1480 (1992).
[7] R. Baier, D. Schiff, and B. G. Zakharov, Annu. Rev. Nucl. Part. Sci. **50**, 37 (2000).
[8] N. Armesto *et al*., Phys. Rev. C **86**, 064904 (2012).
[9] P. Arnold, G. D. Moore, and L. G. Yaffe, J. High Energy Phys. 11 (2001) 057.
[10] X.-N. Wang and X. Guo, Nucl. Phys. A **696**, 788 (2001).
[11] C. A. Salgado and U. A. Wiedemann, Phys. Rev. D **68**, 014008 (2003).
[12] C. Marquet and T. Renk, Phys. Lett. B **685**, 270 (2010).
[13] A. Adare *et al*. (PHENIX Collaboration), Phys. Rev. C **80**, 024908 (2009).
[14] S. S. Adler *et al*. (PHENIX Collaboration), Phys. Rev. C **76**, 034904 (2007).
[15] S. Afanasiev *et al*. (PHENIX Collaboration), Phys. Rev. C **80**, 054907 (2009).
[16] A. Adare *et al*. (PHENIX Collaboration), Phys. Rev. Lett. **105**, 142301 (2010).
[17] A. Adare *et al*. (PHENIX Collaboration), Phys. Rev. Lett. **101**, 232301 (2008).
[18] E. Richardson *et al*. (PHENIX Collaboration), Nucl. Instrum. Methods Phys. Res., Sect. A **636**, 99 (2011).
[19] K. Adcox *et al*. (PHENIX Collaboration), Nucl. Instrum. Methods Phys. Res., Sect. A **499**, 469 (2003).
[20] R. J. Glauber, *Lectures in Theoretical Physics*, edited by W. E. Brittin (Interscience Publishers, New York, 1958).
[21] M. N. Miller, K. Reygers, J. Sanders, and P. Steinberg, Annu. Rev. Nucl. Part. Sci. **57**, 205 (2007).
[22] B. Alver *et al*. (PHOBOS Collaboration), Phys. Rev. Lett. **98**, 242302 (2007).
[23] S. Afanasiev *et al*. (PHENIX Collaboration), Phys. Rev. C **80**, 024909 (2009).
[24] A. Adare *et al*. (PHENIX Collaboration), Phys. Rev. Lett. **109**, 122302 (2012).
[25] M. Chiu (PHENIX Collaboration), AIP Conf. Proc. **915**, 539 (2007).
[26] A. Kazantsev (PHENIX Collaboration), AIP Conf. Proc. **351**, 539 (2007).
[27] L. Aphecetche *et al*. (PHENIX Collaboration), Nucl. Instrum. Methods Phys. Res., Sect. A **499**, 521 (2003).
[28] GEANT 3.2.1, CERN Program Library (1993), http://wwwasdoc.web.cern.ch/wwwasdoc/pdfdir/geant.pdf.
[29] A. Adare *et al*. (PHENIX Collaboration), Phys. Rev. C **77**, 064907 (2008).
[30] A. Adare *et al*. (PHENIX Collaboration), Phys. Rev. C **82**, 011902 (2010).
[31] A. Adare *et al*. (PHENIX Collaboration), Phys. Rev. D **76**, 051106 (2007).
[32] S. S. Adler *et al*. (PHENIX Collaboration), Phys. Rev. Lett. **96**, 202301 (2006).
[33] T. Sjostrand *et al*., Comput. Phys. Commun. **135**, 238 (2001).
[34] C. A. Aidala, F. Ellinghaus, R. Sassot, J. P. Seele, and M. Stratmann, Phys. Rev. D **83**, 034002 (2011).
[35] A. Adare *et al*. (PHENIX Collaboration), Phys. Rev. C **85**, 064914 (2012).
[36] S. Afanasiev *et al*. (PHENIX Collaboration), Phys. Rev. Lett. **99**, 052301 (2007).
[37] S. A. Bass, C. Gale, A. Majumder, C. Nonaka, G. Y. Qin, T. Renk, and J. Ruppert, Phys. Rev. C **79**, 024901 (2009).
[38] K. Aamodt *et al*. (ALICE Collaboration), Phys. Lett. B **696**, 30 (2011).
[39] W. A. Horowitz and M. Gyulassy, Nucl. Phys. A **872**, 265 (2011).
[40] B. Abelev *et al*. (ALICE Collaboration), Phys. Rev. Lett. **105**, 252301 (2010).
[41] H. Appelshauser (ALICE Collaboration), J. Phys. G **38**, 124014 (2011).
[42] A. Adare *et al*. (PHENIX Collaboration), Phys. Rev. Lett. **109**, 202301 (2012).
[43] P. Arnold, G. D. Moore, and L. G. Yaffe, J. High Energy Phys. 06 (2002) 030.
[44] J. Qiu and G. Sterman, Nucl. Phys. B **353**, 105 (1991).
[45] R. Baier, Y. L. Dokshitzer, A. H. Mueller, S. Peigne, and D. Schiff, Nucl. Phys. B **483**, 291 (1997).
[46] B. Zakharov, JETP Lett. **65**, 615 (1997).
[47] A. Majumder, B. Muller, and S. Mrowczynski, Phys. Rev. D **80**, 125020 (2009).
[48] H. Liu, K. Rajagopal, and U. A. Wiedemann, Phys. Rev. Lett. **97**, 182301 (2006).
[49] F. Dominguez, C. Marquet, A. Mueller, B. Wu, and B.-W. Xiao, Nucl. Phys. A **811**, 197 (2008).
[50] J. Jia and R. Wei, Phys. Rev. C **82**, 024902 (2010).
[51] A. Adare *et al*. (PHENIX Collaboration), Phys. Rev. C **84**, 044905 (2011).